ELECTROCHEMISTRY

Acidic-alkaline tandem system for durable CO_2-CO-C_{2+}

Xianhui Ma[1,2]†, Juan Zhang[3]†, Dayin He[1,2], Wei Jiang[1,2], Yuanhua Sun[4], Jiayi Cui[5], Cai Chen[6], Yue Lin[7], Tao Yao[4], Huang Zhou[1,2]*, Yafei Li[3]*, Yuen Wu[1,2]*

Tandem carbon dioxide reduction reaction (CO_2RR) to multicarbon products (CO_2-CO-C_{2+}) such as ethylene represents a pivotal strategy for carbon valorization. However, conventional alkaline or neutral tandem systems limit the carbon dioxide utilization and stability due to severe (bi)carbonate formation. Here, we design a durable acidic-alkaline tandem system to efficiently synthesize C_{2+} products, especially ethylene. In the acidic CO_2RR step, a catalyst with precisely controlled metal site distance was used to regulate *COOH adsorption. Typically, a 99.7 ± 0.4% carbon monoxide Faradaic efficiency (FE) at 1.4 amperes per square centimeter can be achieved using a catalyst with 0.5-nanometer nickel sites, surpassing the previously reported metal catalysts. When this catalyst was integrated into the acidic-alkaline tandem system and coupled with the alkaline carbon monoxide electroreduction, the ethylene and C_{2+} FE reached 75.3 ± 1.2 and 92.5 ± 1.3% at 10 amperes, respectively, and remained stable for 400 hours. Our work provides solutions for the durable conversion of carbon dioxide to C_{2+} products from catalyst and electrolyzer design.

INTRODUCTION

The electrocatalytic carbon dioxide reduction reaction (CO_2RR), which transforms CO_2 into value-added multicarbon feedstocks such as ethylene (C_2H_4) using renewable electricity, has emerged as a transformative platform for sustainable chemical synthesis (*1*–*4*). Current CO_2-to-C_{2+} conversion strategies primarily adopt two configurations: single-step direct electrolysis and two-step tandem electrolysis systems. Single-step CO_2 electrolysis faces several hurdles, including the formation of inevitable carbonate issue, which has a serious impact on stability, limitations in CO_2 utilization, and relatively low selectivity toward a certain type of C_{2+} product under alkaline/neutral conditions (pH ≥ 7) (fig. S1A). In acidic medium (pH < 4), although the precipitation of carbonates can be reduced and the utilization rate of CO_2 can be improved, the single-step production of C_{2+} has the problems of more intense catalyst degradation and enhanced competitive hydrogen evolution reaction (HER), which leads to poor stability and low C_{2+} selectivity (fig. S1B). The two-step tandem electrolysis (CO_2-to-CO-to-C_{2+}) provides a route for improving stability and high carbon product generation (*5*–*8*). In this system, CO_2 is first converted to CO in a CO_2 electrolyzer, and then CO is converted to C_{2+} products in a following carbon monoxide reduction reaction (CORR) electrolyzer. Unlike CO_2, the chemical inertness of CO toward OH^- avoids the formation of carbonate, thereby enhancing reaction stability (*9*–*11*). The CO molecule, as a key intermediate in the preparation of C_{2+} products from CO_2, exhibits favorable kinetics in the production of C_{2+} species, especially in alkaline medium, thereby achieving higher C_{2+} Faradaic efficiency (FE) (*12*–*14*). The more controllable surface coverage of *H and *CO during CORR is conducive to improving the selectivity for individual C_{2+} products.

Although two-step tandem CO_2 electrolysis presents notable potential for C_{2+} production, the current tandem systems mostly use alkaline or neutral electrolytes. The following disadvantages still exist when using these electrolytes to supply CO in the first step (Fig. 1A): (i) Gaseous CO_2 reacts with OH^- ions to form (bi)carbonate, which leads to flooding of the gas diffusion electrodes (GDEs), ultimately reducing the stability of the first step of the tandem system (*15*, *16*); (ii) Substantial CO_2 crossover occurs as (bi)carbonate species, resulting in catastrophic carbon loss [single-pass carbon efficiency (SPCE) < 25%] that severely compromises process economics (*16*, *17*). Operating the CO_2-to-CO part of the tandem system in an acidic system can help solve the above problems (*13*, *18*, *19*) (Fig. 1B) but introduces additional challenges: (i) The proton-rich environments exacerbate the degradation of metal catalysts, making it difficult to achieve long-term operation (*20*, *21*); (ii) The enhanced HER kinetics under strongly acidic environment suppresses *COOH intermediate coverage critical for CO generation (*22*, *23*). Therefore, it is necessary to develop advanced electrocatalysts with high CO_2RR stability and activity in acidic environments to efficiently synthesize CO for tandem systems.

Here, we design an acidic-alkaline tandem CO_2 electrolysis system that achieves higher stability and C_{2+} (especially C_2H_4) selectivity than conventional single-step and alkaline-alkaline tandem systems. The reason is that we achieved the adsorption regulation of CO product intermediates by adjusting the distance between catalyst metal sites in the first acidic CO_2RR step, thereby suppressing HER and improving the activity and stability of the tandem system. Taking Ni sites as an example, when the average site distance is controlled at 0.5 nm, the performance can reach a CO FE of 99.7 ± 0.4% at a current density of 1.4 A cm^{-2} and a single-pass conversion rate (SPCE) of 89.9 ± 2.2% at pH = 1, exceeding the performance of the reported metal catalysts. When the catalyst is applied to an acidic-alkaline tandem system, in the first step, a total current of 30 A and a high CO FE of 98.1% are achieved in a 100-cm^2 slim flow cell with a cell

[1]Key Laboratory of Precision and Intelligent Chemistry/School of Chemistry and Materials Science, University of Science and Technology of China, Hefei 230026, China. [2]Deep Space Exploration Laboratory, University of Science and Technology of China, Hefei 230026, China. [3]Jiangsu Key Laboratory of New Power Batteries, Jiangsu Collaborative Innovation Centre of Biomedical Functional Materials, School of Chemistry and Materials Science, Nanjing Normal University, Nanjing 210023, China. [4]National Synchrotron Radiation Laboratory, University of Science and Technology of China, Hefei 230029, China. [5]School of Rare Earths, University of Science and Technology of China, Hefei 230026, China. [6]Institute of Carbon Neutrality, College of Chemistry and Chemical Engineering, Southwest Petroleum University, Chengdu, Sichuan 610500, China. [7]Hefei National Research Center for Physical Sciences at the Microscale, University of Science and Technology of China, Hefei 230026, China.
*Corresponding author. Email: huangz02@ustc.edu.cn (H.Z.); liyafei@njnu.edu.cn (Y. Li); yuenwu@ustc.edu.cn (Y.W.)
†These authors contributed equally to this work.

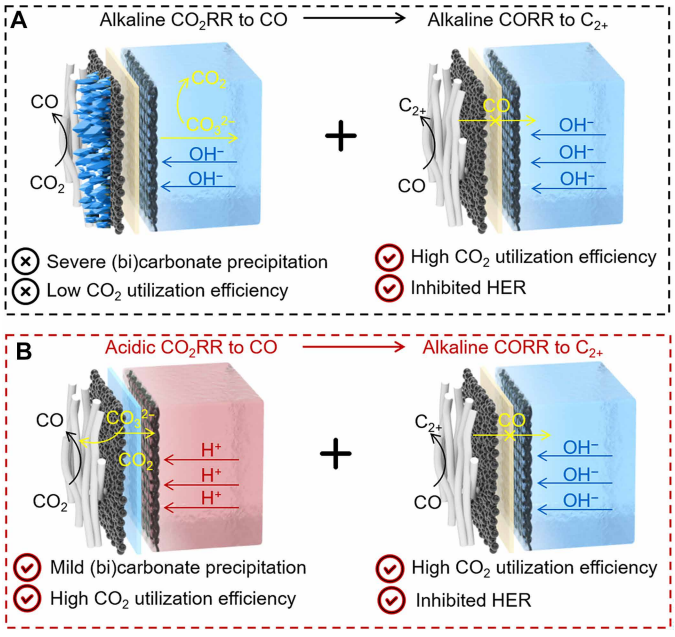

Fig. 1. Schematic of different CO_2RR systems. (**A**) Schematic of alkaline or neutral CO_2RR and alkaline CORR tandem system. (**B**) Schematic of acidic CO_2RR and alkaline CORR tandem system.

potential of only 2.85 V. In the second step, based on a modified CuO catalyst, alkaline CORR achieves 92.5 ± 1.3% C_{2+} FE and 75.3 ± 1.2% C_2H_4 FE at a total current of 10 A. Moreover, our system can achieve more than 400 hours of durable operation without any carbonate issue, which exceeds the performance of single-step and alkaline-alkaline tandem CO_2RR systems. In situ electrochemical spectroscopy and density functional theory (DFT) calculations reveal that Ni sites with optimal interatomic distance promote the adsorption of *COOH intermediates and the CO_2-assisted stabilization mechanism of Ni-N_3V sites under acidic CO_2RR conditions. Further technoeconomic analysis (TEA) shows that in the case of further reduction of electricity prices in the future, the cost of C_2H_4 production by the acidic-alkaline CO_2 tandem system is only $1272.3/ton, which is lower than the commercial price of oil-to-C_2H_4 ($1350/ton), and will be expected to replace the traditional C_2H_4 synthesis route.

RESULTS

Technoeconomic analysis

We first perform TEA to evaluate the feasibility of existing CO_2RR systems including single-step direct CO_2RR system (alkaline or acidic CO_2RR) and tandem CO_2RR system (alkaline-alkaline or acidic-alkaline CO_2RR) in terms of C_2H_4 production costs. The key electrolyzer parameters that affect the final production cost of C_2H_4 produced by different CO_2RR systems are listed in table S1, and the C_2H_4 costs under optimistic and pessimistic scenarios are calculated on the basis of the optimal performance and general performance of the current literature (Fig. 2A). Among them, C_2H_4 directly produced by alkaline CO_2RR system has the highest cost in both pessimistic ($10,441.1/ton) and optimistic ($4989.1/ton) scenarios (table S2), which is much higher than the cost of C_2H_4 produced by the traditional petroleum industry ($1350/ton) (*24*). This is because it is difficult to achieve high FE and SPCE for C_2H_4 produced by alkaline CO_2RR, which increases the cost of electricity and product separation, greatly limiting the industrial prospects of CO_2RR technology. In the optimistic scenario, acidic CO_2RR greatly reduces the anode separation cost due to higher CO_2 SPCE and lower salt precipitation problem, making the cost of C_2H_4 produced by this system ($2347.5/ton) lower than the cost of alkaline CO_2RR and alkaline-alkaline tandem CO_2 electroreduction ($4006.2/ton) (table S3). Satisfactorily, the acidic-alkaline tandem CO_2RR system still has the lowest C_2H_4 cost ($1698.5/ton) because this system overpotential can be reduced by tandem conversion, which reduces the electricity cost by 41.7, 4.3, and 34.5% compared with the alkaline, alkaline-alkaline tandem, and acidic CO_2RR systems, respectively (tables S4 to S6). The acidic-alkaline tandem system completely avoids the cost of anode separation under ideal conditions. Figure 2B shows that under optimistic and pessimistic scenarios, the cost of preparing CO by acidic CO_2RR is $590.9/ton and $1201.5/ton, respectively, accounting for 37.4 and 62.6% of the acidic-alkaline tandem system. The electricity cost accounts for more than 45% of the cost of preparing CO by acidic CO_2RR and C_2H_4 by alkaline CORR (Fig. 2C). Under the optimistic scenario, the electricity cost of acidic CO_2RR accounts for as high as 74.1%. Therefore, reducing the power consumption by lowering the overpotential of the reaction unit will help improve the economic efficiency of C_2H_4 preparation in the acidic-alkaline tandem system. Figure 2 (D to G) indicates that when the electricity price is $0.03 kilowatt-hour $(kWh)^{-1}$ (renewable energy such as wind power), the profitable area continues to expand with the decrease of the electrolyzer potential and the increase of C_2H_4 FE. The acidic-alkaline tandem CO_2RR system has the largest profitable area, while the other three systems are difficult to achieve a break-even line in C_2H_4 cost at extremely low potential and extremely high C_2H_4 FE. These results suggest that the acidic-alkaline tandem CO_2RR system is the most economically feasible and is expected to replace the traditional petrochemical system to produce low-cost C_2H_4 product.

DFT calculations

The key to the operation of the tandem system lies in the catalyst, especially the first step, which requires an efficient acidic CO_2RR catalysts. Previous studies show that single-atom catalysts (SACs) have higher CO selectivity than traditional nanoparticles (*25*–*27*). For example, the CO FE of Ni SACs can reach ~100% under alkaline conditions (*28*–*31*). However, the lower HER energy barrier under strongly acidic conditions increases the instability of SACs. When HER is the dominant reaction under the action of reduction potentials, the strength of the metal-nonmetal bond usually decreases, and the SAC will undergo bond breaking and aggregation (*32*–*37*). When CO_2RR is the dominant reaction on the surface, the enhanced adsorption of CO_2 intermediates (*COOH) at single-atom sites helps slow down the attack of *H on nonmetal sites, preventing the breakage of metal-nonmetal bonds and thus improving the structural stability of the catalysts. Therefore, to achieve durable electroreduction of CO_2 to CO, properly adjusting the adsorption of the *COOH intermediate is very crucial. We preliminarily screened the structures of SACs with the strong *COOH adsorption under acidic conditions (pH = 0) through DFT calculations. Taking Ni as an example, we first constructed a model of Ni SAC including conventional Ni-N_4 and Ni-N_3V (fig. S2, A and B). The activation of the CO_2 to *COOH process shows an uphill free energy change [ΔG(*COOH)] on these structures, indicating that the conversion process of CO_2 to COOH* has

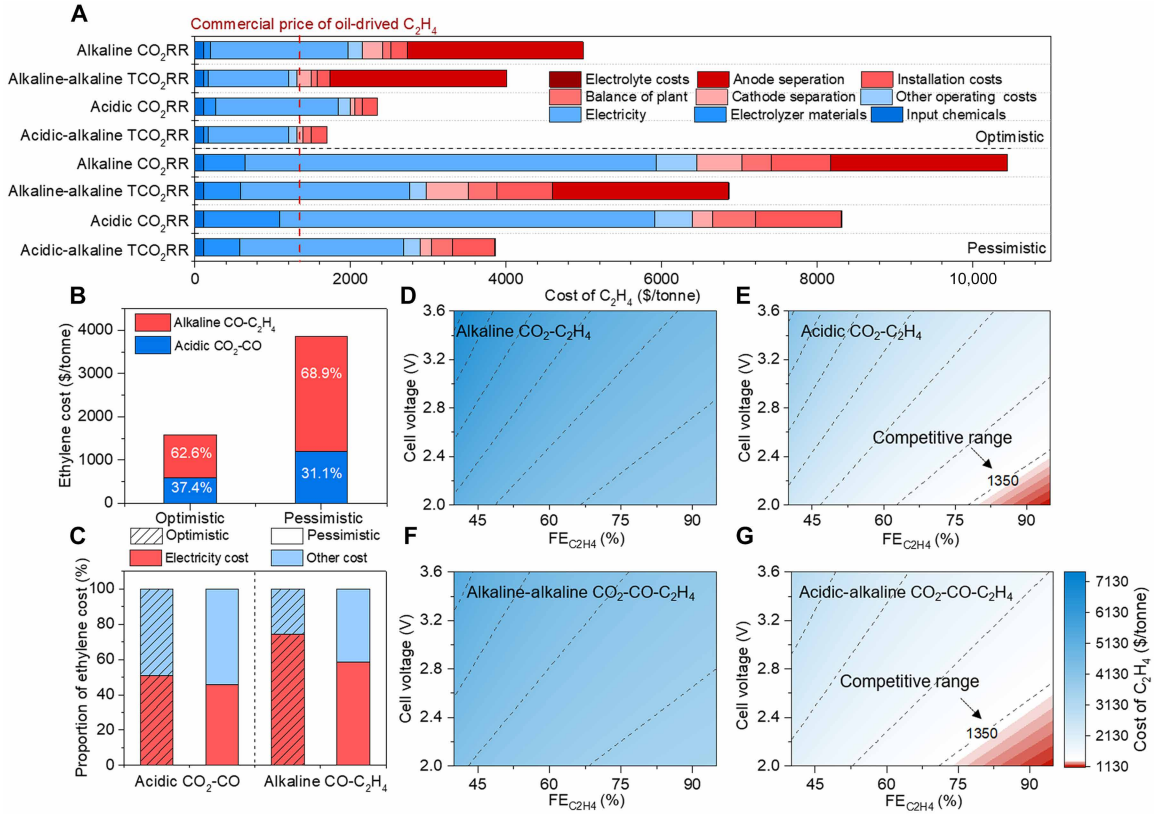

Fig. 2. TEA of different CO_2RR systems. (**A**) Breakdown of the overall process costs for different electroreduction systems under optimistic and pessimistic scenarios at a given electricity price of \$0.03/kWh. The red dashed line shows the current cost of C_2H_4. (**B**) Costs and (**C**) contributions of acidic CO_2RR part and alkaline CORR part under optimistic and pessimistic scenarios. Contour plot of C_2H_4 production cost calculated at different cell potentials and FE for (**D**) alkaline CO_2RR system, (**E**) acidic CO_2RR system, (**F**) alkaline CO_2RR in tandem with alkaline CORR system, and (**G**) acidic CO_2RR in tandem with alkaline CORR at a given electricity price of \$0.03/kWh.

a large energy barrier and is a rate-determining step reaction (fig. S3A). When an additional Ni-N_3V site is introduced at a distance of 1 nm from the Ni-N_3V site (fig. S2C), the ΔG(*COOH) is reduced from 2.07 eV (for Ni-N_4) and 0.86 eV (for Ni-N_3V) to 0.71 eV. This indicates that, compared to the other Ni atomic structures, regulating the distance between Ni-N_3V sites may enhance the CO_2RR performance. In addition, the limiting potential difference [$U_L(CO_2)$-$U_L(H_2)$] of CO_2RR and HER was calculated to consider the thermodynamic selectivity of the reaction. The $U_L(CO_2)$-$U_L(H_2)$ value of the Ni-N_3V-1.0 nm site in fig. S3B is more positive than those of Ni-N_4 and Ni-N_3V, indicating that the adjacent Ni-N_3V site can further improve the selectivity of the Ni-N_3V site for CO_2 to CO. The above results show that by regulating the atomic distance of Ni-N_3V to enhance the adsorption of *COOH, it is expected to achieve CO_2 to CO conversion with high activity and stability under acidic medium (Fig. 3, A and B).

Controllable synthesis and characterizations of Ni SACs with various site distances

A two-step strategy combining polycondensation and subsequent pyrolysis procedures is developed to synthesize Ni SACs with different site distances (fig. S4). The key success of this strategy relies on the controlled polycondensation and coordination in the first step, in which small molecules [Ni precursor, dicyandiamide (DCD), and formaldehyde (HCHO)] are polymerized in hot water in one pot to form coordination polymers coated on the surface of nano silicon dioxide (SiO_2) nanoparticles. Next, the obtained Ni coordination polymer was calcined at high temperature (900°C) in an argon atmosphere to volatilize the N part in the polymer, and SiO_2 is etched away using hydrofluoric acid (HF) to obtain the final Ni SAC. Ni single atoms distributed on nitrogen-doped carbon (NC) with different site distances can be easily obtained by adjusting the amount of metal precursor [the metal loading of 0.5 ± 0.13, 1.3 ± 0.15, 4.5 ± 0.33, and 9.9 ± 0.60 wt % measured by inductively coupled plasma atomic emission spectroscopy (ICP-AES)]. The only broad peak detected in the x-ray diffraction (XRD) pattern of the Ni SAC sample indicates the formation of amorphous NC material in the catalysts (fig. S5).

From the transmission electron microscopy (TEM) and high-resolution transmission electron microscopy (HRTEM) images, it can be seen that these catalysts have graphene layers with abundant mesopores of about 20 nm, and no nanoparticles are observed (fig. S6). In addition, the N_2 adsorption-desorption isotherms and pore size distributions indicate that the NC support has a high specific surface area (>950 $m^2\ g^{-1}$) and rich mesoporous structure (fig. S7 and table S7), which will help improve the mass transfer efficiency of CO_2 and the utilization efficiency of metal sites. Figure S8 shows further high-angle annular dark field scanning transmission electron microscopy (HAADF-STEM) images and corresponding energy-dispersive x-ray (EDX) elemental mapping analysis, from which we

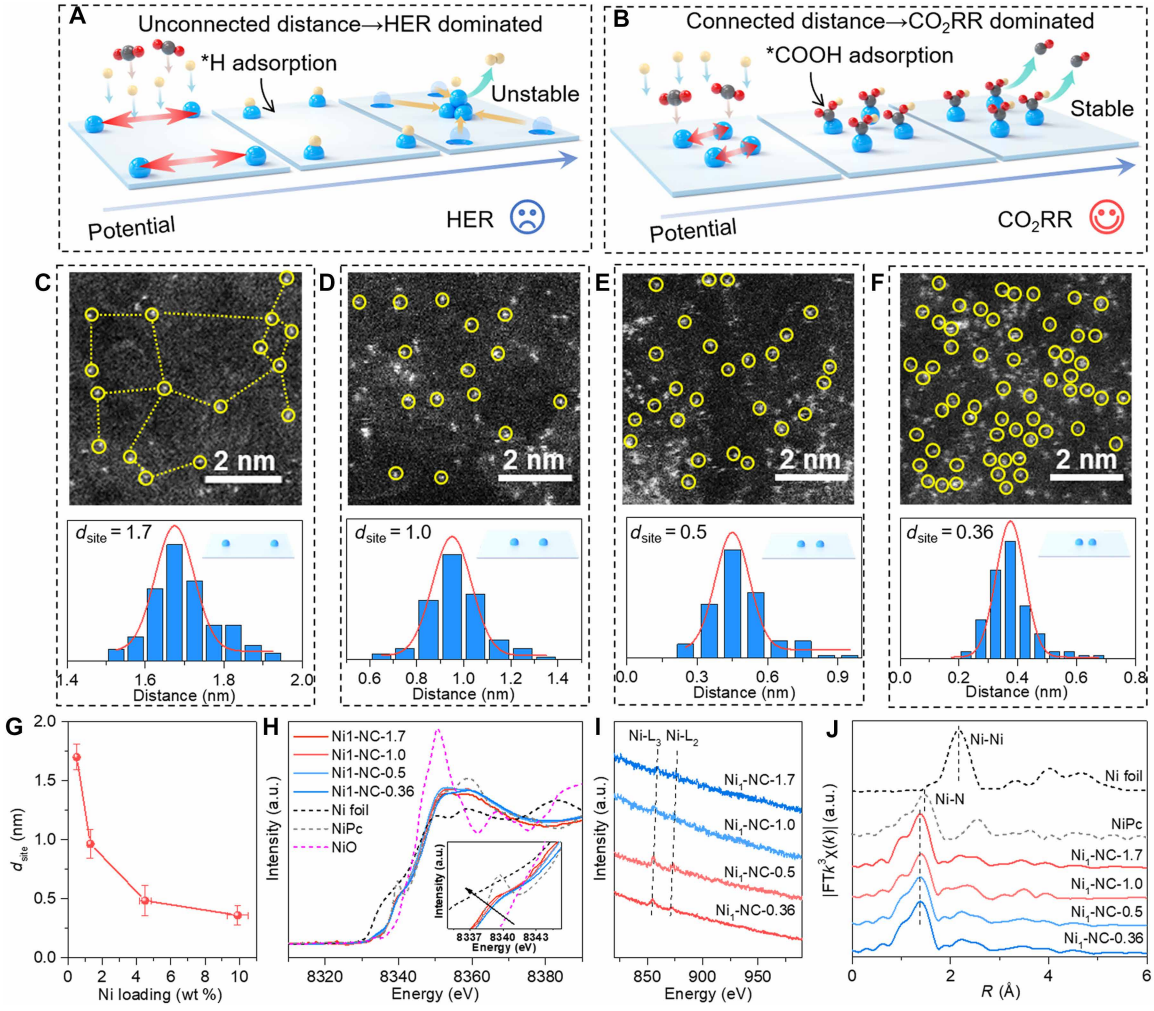

Fig. 3. Characterizations and atomic structural analysis of Ni SACs with different distance. Schematic of the possible structural evolution of single atoms at (**A**) unconnected and (**B**) connected atomic distances dominated by HER and CO_2RR, respectively. (**C** to **F**) Aberration-corrected high-angle annular dark field scanning transmission electron microscopy (AC-HAADF-STEM) images and corresponding distribution of atomic distances of Ni_1-NC-X samples. Ni single atoms are marked in yellow circles. (**G**) Calibration of the distance of Ni sites (d_{site}) with statistical distributions from STEM images against the corresponding Ni loading determined by inductively coupled plasma atomic emission spectroscopy (ICP-AES). The error bars correspond to the SDs of Ni contents (*x* axis) and the d_{site} (*y* axis) for each sample prepared in three independent trials. (**H**) Normalized Ni K-edge x-ray absorption near-edge structure (XANES) spectra. a.u., arbitrary units. (**I**) Electron energy-loss spectroscopy (EELS) of Ni_1-NC-X. (**J**) Fourier transform magnitude function, FT|$k^3\chi(k)$|, of phase-corrected extended x-ray absorption fine structure (EXAFS) spectra of Ni_1-NC-X and reference samples.

can see that C, N, and Ni atoms are uniformly dispersed throughout the structure of these catalysts. The x-ray photoelectron spectroscopy (XPS) survey also detects the presence of the three elements, and the Ni 2p peak is enhanced with the increase of Ni loading (fig. S9A). As shown in Fig. 3 (C to F), aberration-corrected HAADF-STEM (AC-HAADF-STEM) images show that the Ni species are all atomically dispersed, and the distance of Ni sites (d_{site}) decreases with the metal loading increases. The average d_{site} is determined using calculated statistics from AC-HAADF-STEM images of all samples (these catalysts are named Ni_1-NC-X; X represents the d_{site} of 1.7, 1.0, 0.5, and 0.36 nm). To increase the reliability of the measurement, we considered signals from more than 50 atoms collected by AC-HAADF-STEM images for each catalyst. The statistical method used in this study to estimate the d_{site} only examines regions with very thin thickness, where all Ni atoms can be counted. Thicker regions are ignored because STEM imaging cannot easily record enough atoms within the required resolution. Figure 3G shows an inverse correlation between Ni site distances and metal loading, with d_{site} systematically decreasing from 1.7 to 0.36 nm, as the Ni content increases from 0.5 to 9.9 wt % (table S8).

X-ray absorption spectroscopy (XAS) measurements were then performed to investigate the electronic properties and coordination structures of these Ni SACs with different site distances. Figure 3H shows the normalized Ni K-edge x-ray absorption near-edge structure (XANES) spectra. It can be seen that the absorption threshold position is located between NiO and Ni foil, indicating that the valence of the Ni species is between 0 and +2. However, the position of the rising edge decreases from Ni_1-NC-1.7 to Ni_1-NC-0.36, indicating that the Ni oxidation state becomes lower with increasing Ni site distance. These results are also confirmed by the electron energy-loss spectroscopy (EELS) of Ni-L (Fig. 3I) and Ni 2p XPS (fig. S9B). This suggests a more reductive state for Ni, which probably is induced

by the electronic interaction between adjacent sites. The corresponding extended x-ray absorption fine structure (EXAFS) spectra show that Ni—N has only one prominent peak at ~1.52 Å, while there is no Ni—Ni peak at ~2.2 Å (Fig. 3J), confirming the presence of atomically dispersed metal atoms in the Ni_1-NC-X samples. The first shell theoretical fitting of the EXAFS spectra using the Ni-N_3V model can fit the four samples well. The corresponding parameters in table S9 show that the coordination numbers (CN) of the four representative samples are 3.1 to 3.3, which means that the Ni-N_3V part is dominant in the samples with different d_{site} values. The room-temperature electron paramagnetic resonance (EPR) of Ni_1-NC-0.36 reveals the coordinatively unsaturated state of Ni species, demonstrating the existence of N vacancies (fig. S10). The wavelet transform images also show that there is only one maximum intensity on the Ni—N scattering path, located at ~5 $Å^{-1}$ (fig. S11). These results indicate that these Ni SACs can maintain the same Ni-N_3V coordination structure except for the different site distances. In other words, the transition of Ni valence states and the different electronic structures of the central Ni atom should be attributed to the different site distances in these Ni SACs rather than the coordination structure or CN.

In addition, to demonstrate the universality of site distance regulation, four SACs were synthesized by replacing the Ni precursor with nitrates of Fe, Co, Cu, and Zn (table S10). TEM images (fig. S12) and EDX mapping (fig. S13) demonstrate the absence of corresponding nanoparticles in the above catalysts and the uniform distribution of the elements. Figure S14 shows that no metal peaks are observed in XRD pattern. Similarly, the loading and site distance of each catalyst are quantified by ICP-AES and AC-HAADF-STEM (fig. S15), respectively. These catalysts are named Fe_1-NC-0.81, Fe_1-NC-0.42, Co_1-NC-0.97, Co_1-NC-0.4, Cu_1-NC-0.9, Cu_1-NC-0.41, Zn_1-NC-0.89, and Zn_1-NC-0.46 according to the site distance.

Regulation of electrochemical CO_2RR performance

To verify whether regulating the site distance of SACs would have a positive effect on CO_2RR, we conducted CO_2RR performance tests in a three-chamber flow cell containing 3 M KCl (pH adjusted to 1 by concentrated H_2SO_4). Figure 4A shows that Ni_1-NC-0.5 has enhanced CO_2RR activity compared with Ni_1-NC-1.7, Ni_1-NC-1.0, and Ni_1-NC-0.36 over the entire applied potential. At a current density of 1.4 A cm^{-2}, Ni_1-NC-0.5 shows the best CO_2 to CO generation, with an FE of 99.7 ± 0.4%, while the FE_{CO} values of Ni_1-NC-1.7,

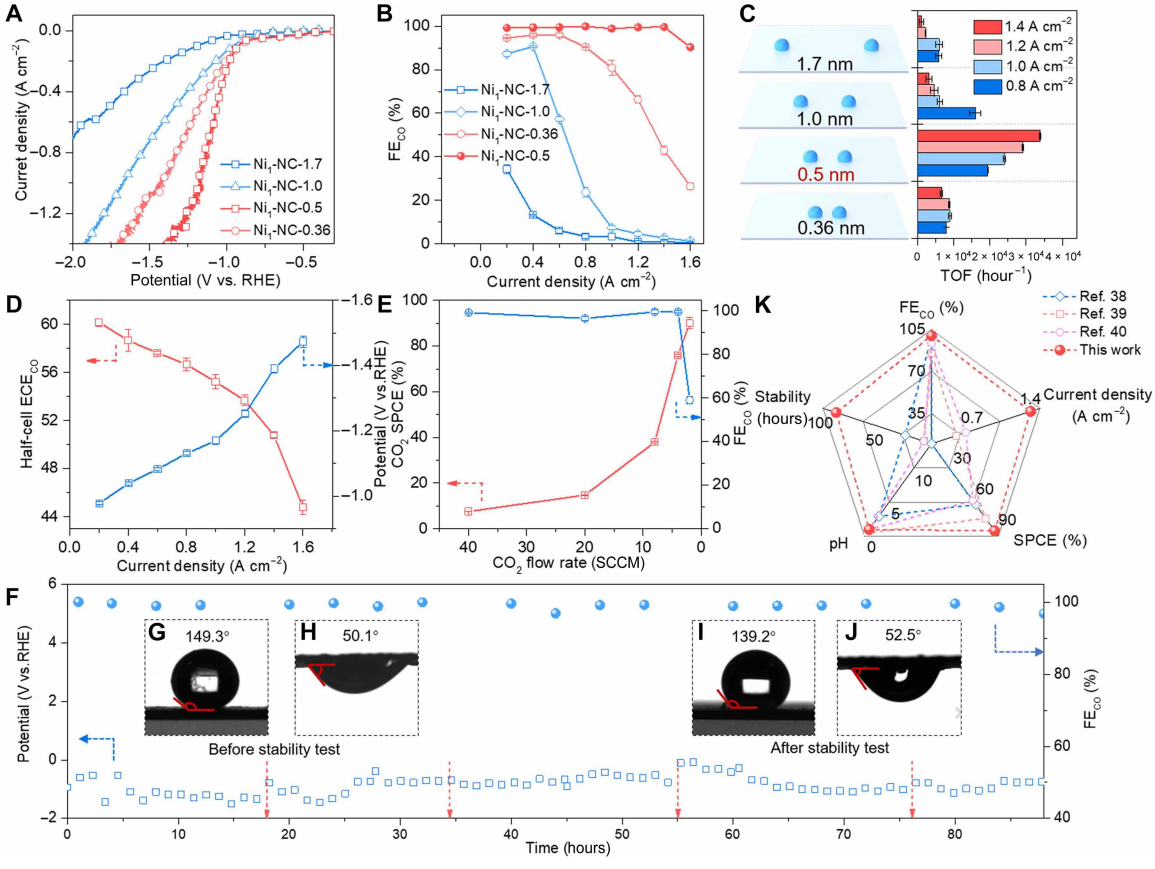

Fig. 4. CO_2RR performance evaluation of Ni_1-NC-X catalysts. (**A**) The corresponding current density at different applied potentials in flow cell with flowing 3 M KCl (the pH value was adjusted to be 1 by H_2SO_4) electrolytes. (**B**) FE_{CO} of Ni_1-NC-X at different current densities. (**C**) Schematic diagram of catalysts with different atomic distance and their corresponding TOF. (**D**) CO half-cell ECE and partial current density of Ni_1-NC-0.5 catalyst at different potentials. (**E**) The CO_2 SPCE of and CO FE of Ni_1-NC-0.5 catalyst at different CO_2 flow rates at a current density of 0.4 A cm^{-2}. (**F**) The stability measurement of CO product FE with an applied current density of 0.6 A cm^{-2}. The red dashed arrows mark the time of refreshing the electrolyte. (**G**) Liquid and (**H**) gas contact angle of Ni_1-NC-0.5 electrode before stability test. (**I**) Liquid and (**J**) gas contact angle of Ni_1-NC-0.5 electrode after stability test. (**K**) Comparison of CO_2RR current density, CO product FE, stability, pH of bulk electrolyte, and SPCE of Ni_1-NC-0.5 with state-of-art CO_2RR catalysts.

Ni_1-NC-1.0, and Ni_1-NC-0.36 are 0.87 ± 0.7, 2.7 ± 0.6, and 43.0 ± 2.1%, respectively, due to the increase in HER (Fig. 4B). Moreover, the linear sweep voltammetry curves of Ni catalysts with different atomic distances measured using a rotating disk electrode in an Ar atmosphere indicate that Ni_1-NC-0.5 exhibits the highest HER overpotential and the lowest current density at the same potential (fig. S16), similarly suggesting its poorest HER performance, which might contribute to the stability of Ni sites under acidic conditions. The electrochemical surface area (ECSA) analysis (fig. S17, A to E) shows that the ECSA of Ni_1-NC-0.5 is comparable to that of other catalysts, suggesting that the performance improvement is not solely due to an increase in surface area. Furthermore, the ECSA-normalized CO current density indicates that Ni_1-NC-0.5 exhibits the highest current density, achieving 100.2, 43.1, and 2.2 times higher values than Ni_1-NC-1.7, Ni_1-NC-1.0, and Ni_1-NC-0.36, respectively, at 1.4 A cm^{-2} (fig. S17F). This demonstrates that tuning the interatomic distance enhances the intrinsic activity of the Ni sites. In addition, we further evaluate the turnover frequency (TOF) of Ni_1-NC-X (Fig. 4C). The results show that the Ni_1-NC-0.5 catalyst exhibits a TOF of 33852.6 ± 139.7 $hour^{-1}$ at a current density of 1.4 A cm^{-2} and a TOF of 35184.8 ± 462.7 $hour^{-1}$ at a current density of 1.6 A cm^{-2}, which are notably higher than those of other catalysts, indicating the highest intrinsic activity. The improvement in catalytic activity may be attributed to the regulation of the electronic structure of the site distance between Ni sites. Figure 4D shows that the Ni_1-NC-0.5 catalyst has a half-cell energy conversion efficiency (half-cell ECE_{CO}) of 60.2 ± 0.3% at a current density of 0.2 A cm^{-2}. In contrast, the corresponding half-cell ECE_{CO} values of Ni_1-NC-1.7, Ni_1-NC-1.0, and Ni_1-NC-0.36 catalysts at the same current density are only 17.3 ± 1.0, 50.6 ± 0.7, and 58.4 ± 0.6%, respectively (fig. S18). Moreover, with the increase of current density, the increase of overpotential leads to a gradual decrease in half-cell ECE_{CO}. Because acidic CO_2RR reduces the conversion and crossover of CO_2 to carbonates and generally has a high single-pass conversion efficiency (SPCE), we further evaluate the CO_2 SPCE of Ni_1-NC-0.5 at a current density of 0.4 A cm^{-2}. Figure 4E shows that when the CO_2 flow rate is 2.0 standard cubic centimeter per minute (SCCM), the SPCE reaches 89.9 ± 2.2%, and the FE of CO is 59.0 ± 1.6%. Figure 4F shows that when CO_2 electrolysis is carried out at a constant current density of 1.0 A cm^{-2}, the potential of Ni_1-NC-0.5 is stabilized at 1.08 ± 0.3 V versus reversible hydrogen electrode (RHE), and the CO FE is stabilized at 99.1 ± 0.8% for a duration of 88 hours. The liquid contact angle of the GDE for 3 M KCl (pH = 1) electrolyte (149.3° versus 139.2°) and the gas contact angle for CO_2 (50.1° versus 52.5°) before and after the reaction are almost unchanged (Fig. 4, G to J), indicating that GDE maintains good hydrophobic and aerophilic stability. After the stability test, no carbonate precipitation is observed on the back of the carbon paper, which also illustrates the stability of GDE in acidic solution (fig. S19). In addition, the EXAFS spectra of Ni_1-NC-0.5 after 88 hours of reaction are fitted, and the CN is 3.35, which is consistent with that before the reaction (fig. S20 and table S11). The performance of the Ni_1-NC-0.5 catalyst is compared with the reported state-of-the-art acidic CO_2RR electrocatalysts (Fig. 4K) (*38*–*40*), which surpasses the previous catalysts in terms of current density, CO FE, stability, and CO_2 SPCE (table S12). The above results indicate that this catalyst optimized by site distance regulation is highly likely to be applied in the acidic-alkaline tandem CO_2RR system.

To verify the universality of the distance effect, we further tested the CO FE and TOF of other metal SACs at different site distances. The results show that adjusting the distance between metal sites for different metal elements affects the performance of acidic CO_2RR. Compared with Fe_1-NC-0.81, Co_1-NC-0.97, Cu_1-NC-0.9, and Zn_1-NC-0.89, the CO FE of Fe_1-NC-0.42, Co_1-NC-0.4, Cu_1-NC-0.41, and Zn_1-NC-0.46, at a current density of 0.1 A cm^{-2} increased by 12, 53, 22, and 45%, respectively (fig. S21). In the current density range of 0.05 to 0.3 A cm^{-2}, the TOF of catalysts with closer metal sites is higher than that of catalysts with farther metal sites, indicating that adjusting the atomic distance can effectively affect the CO_2RR activity of the site. In addition, by adjusting the metal composition and current density, syngas with a H_2/CO ratio ranging from 0.25 to 13.3 can be produced (fig. S22).

Mechanism of Ni site distance effect

To reveal how the distance effect of Ni sites affects the activity and stability of CO_2RR under acidic medium, we used a series of in situ electrochemical characterizations to monitor the changes in the intermediates and catalyst structures. We used in situ electrochemical surface-enhanced Raman spectroscopy (SERS) to monitor the key intermediates in CO_2RR over Ni_1-NC-0.5 and Ni_1-NC-1.0 catalysts (fig. S23). Figure 5A shows that only peaks A at 1368 cm^{-1} and D at 1600 cm^{-1} are observed under open circuit potential (OCP), which are attributed to the D and G peaks of the carbon substrate and remained unchanged during the reaction. After applying a reduction potential, two obvious peaks appear. Peaks B (~1396 cm^{-1}) and C (~1532 cm^{-1}) are assigned to the C—O bond and asymmetric O—C—O^- stretching of the *COO^- intermediate, respectively (*41*, *42*). The shift of bands associated with the applied potential is caused by the Stark tuning effect. Weaker adsorption of *COO^- intermediates is observed for Ni_1-NC-1.0 compared to Ni_1-NC-0.5 catalyst (fig. S24). This suggests that the appropriate Ni site distance may improve the performance by enhancing the adsorption of CO_2 intermediates. In addition, two peaks are monitored at 1397 and 1698 cm^{-1} by in situ attenuated total reflection Fourier transform infrared (ATR-FTIR) (Fig. 5B and fig. S25), which are attributed to the C—O bond and C═O bond of the *COOH intermediate, respectively (*43*, *44*). No *CO peak is observed, which is usually at 2000 to 2100 cm^{-1}, due to the weak CO adsorption on the Ni site. This feature favors the generation of CO and prevents its deep reduction. The potential-dependent CO_2RR activity is also manifested by the increase in the intensity of the steady-state *COOH peak when the potential is scanned from −0.4 to −1.4 V. Compared with the Ni_1-NC-1.0 catalyst, the peak of the *COOH intermediate is much lower than that of Ni_1-NC-0.5 at the same potential (fig. S26). These ATR-FTIR results indicate that the rational adjustment of the atomic distance of the Ni site can enhance the *COOH adsorption and contribute to the CO_2RR process driven by the catalyst.

We further measured in situ XAS using a homemade flow cell with GDE in the electrolyte at pH = 1 (fig. S27) to monitor the structural stability of catalysts. Figure 5C shows the XANES spectra at different potentials. Compared with the OCP condition, the position of the absorption edge shifts to lower energy after applying the CO_2RR potential. These results reveal that the oxidation state of the atomically dispersed Ni sites decreases with increasing overpotential during CO_2RR. This may be due to the strong electronic interaction between the NC-supported Ni-N_3V sites and the surface-adsorbed

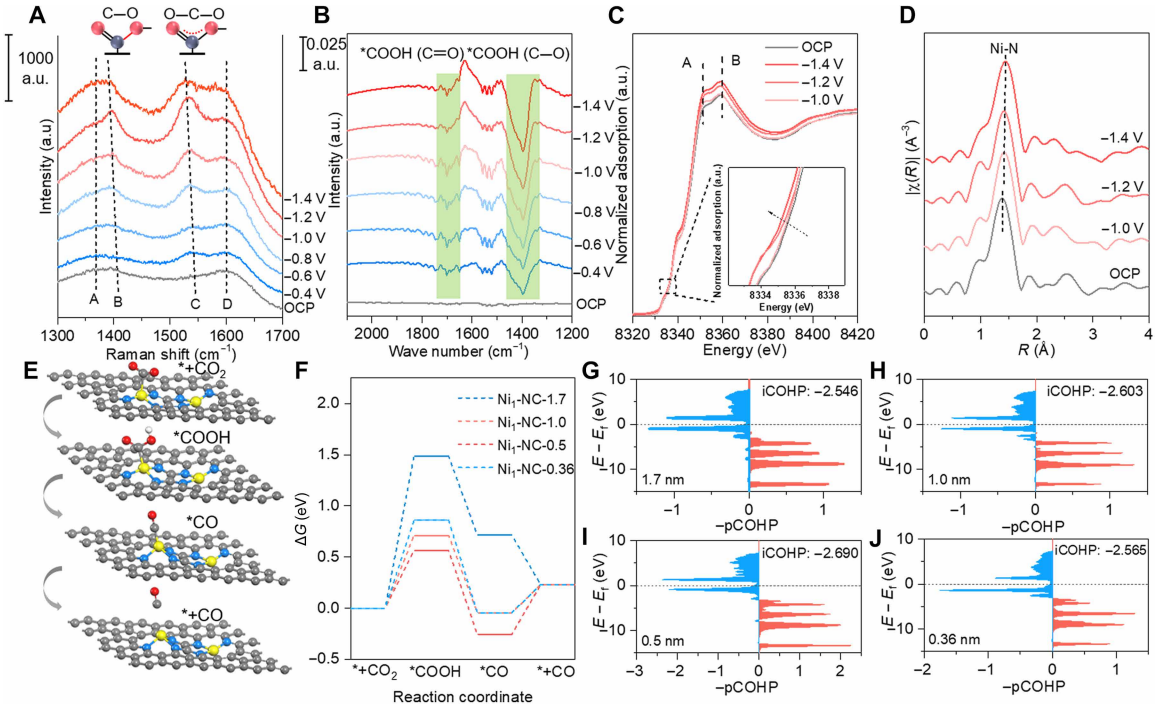

Fig. 5. In situ characterizations and DFT calculations for CO product enhancement mechanism. (**A**) In situ SERS of Ni_1-NC-0.5 electrode during CO_2 reduction reaction under different potentials. The red and gray balls represent O and C, respectively. (**B**) In situ ATR–surface-enhanced infrared absorption spectroscopy (SEIRAS) of Ni_1-NC-0.5 electrode during CO_2 reduction reaction under different potentials. In situ Ni K-edge (**C**) XANES spectra and (**D**) EXAFS spectra of Ni_1-NC-0.5 catalyst in a flow cell electrolyzer at different applied potentials. (**E**) The catalytic pathway on Ni-N_3V based on the *COOH and *CO adsorption intermediates after optimization. Yellow, blue, black, and white spheres represent Ni, N, C, and H atoms, respectively. (**F**) Calculated free energy profile of CO_2RR intermediates on different models at pH = 0. The negative projected crystal orbital Hamiltonian population (−pCOHP) of the Ni—C bond for *COOH adsorption on (**G**) Ni_1-NC-1.7, (**H**) Ni_1-NC-1.0, (**I**) Ni_1-NC-0.5, and (**J**) Ni_1-NC-0.36.

C-containing intermediates, leading to the formation of low-valent Ni sites, which promotes CO_2 activation and CO generation. In addition, we can find that the intensity of peak A increases slightly, while the intensity of peak B decreases slightly. This change can be tracked by the I_A/I_B ratio (*45*, *46*). When a *COOH binds to the nickel site, the nickel atom protrudes from the Ni-N_3V plane, resulting in an increase in I_A/I_B (fig. S28A). The I_A/I_B value of the Ni_1-NC-0.5 catalyst at different potential has almost no change, indicating that the Ni site of Ni_1-NC-0.5 binds *COOH intermediates strongly. The in situ EXAFS shows that the radial distance of the Ni—N peak under OCP conditions is ~1.857 Å, but it shows a positive shift of 1.859, 1.86, and 1.875, respectively, when the applied potential is −1.0 to −1.4 V (Fig. 5D and fig. S28B), indicating that the Ni—N bond is extended under CO_2RR. The CN of Ni_1-NC-0.5 is 3.3 at OCP, and CN increases with the increase of applied potential (table S13). The highest CN is close to 4.0 at −1.4 V, which is due to the combination of *COOH intermediates with Ni-N_3V sites, resulting in an increase in CN. The in situ EXAFS results demonstrate the distortion of Ni atoms away from the carbon plane and the redistribution of electrons in the Ni 3d orbitals, which enhances the interaction between the Ni sites and the CO_2RR intermediates. No Ni—Ni bond is observed in the in situ EXAFS fitting, which indicates that the Ni sites still exist in the form of isolated Ni single atom during CO_2RR process. To further demonstrate the stability of the catalyst structure, we used a series of ex situ electron microscopy characterizations to observe the state after CO_2RR testing at −1.4 V. Figure S29 shows that no nanoparticles are observed in the ex situ TEM, HRTEM, and EDX mapping, and the ex situ AC-HAADF-STEM also shows that the average atomic distance of Ni sites is still 0.53 nm (fig. S30). However, in the in situ XANES spectra, the applied cathodic potential (−1.4 V) causes a decrease in both the absorption edge energy and the white line intensity for Ni_1-NC-1.0 catalyst (fig. S31A). At the same time, a characteristic peak of Ni—Ni (2.48 Å) gradually emerged in the in situ EXAFS. The fitting results show that the CN of Ni—N is 1.34 and the bond length is 1.89 Å (fig. S31B), indicating that bond stretching and breaking of the Ni—N bond occur in the Ni_1-NC-1.0 catalyst. These features indicate that appropriately adjusting the atomic distance may help enhance the stability of Ni-N_3V sites during the acidic CO_2RR process. Moreover, the ex situ HRTEM and AC-HAADF-STEM images show the appearance of irregular Ni nanoparticles below 10 nm and the reduction in the number of Ni sites on NC (figs. S32 and S33). These indicate that the atomic structure of Ni_1-NC-1.0 catalyst is unstable under acidic conditions, and dissolution and agglomeration of Ni sites occur during the CO_2RR process. The above results indicate that the appropriate Ni-N_3V site distance can help improve the selectivity and stability of the catalyst for acidic CO_2RR, which is also supported by the following theoretical calculations.

To further theoretically reveal the optimization effect of CO_2RR performance under different Ni site distances, we further constructed four catalyst models with different Ni-N_3V atomic distances and optimized the adsorption models of different intermediates in the

process of CO_2 conversion to CO ($CO_2 \rightarrow$ *COOH $\rightarrow$ *CO $\rightarrow$ CO) (Fig. 5E). Figure 5F shows that the energy barrier (0.56 eV) of *COOH formation of Ni_1-NC-0.5 is lower than that of Ni_1-NC-1.7 (1.49 eV), Ni_1-NC-1.0 (0.86 eV), and Ni_1-NC-0.36 (0.71 eV) (fig. S34). Moreover, the model of Ni_1-NC-0.5 has the highest HER barrier compared with other site distances (fig. S35). The above results prove that the catalyst has a low starting potential and high CO_2RR selectivity, which is consistent with the experimentally measured performance. The $U_L(CO_2)$-$U_L(H_2)$ value of Ni_1-NC-0.5 with a site distance of 0.5 nm is more positive than that of other models, indicating that this structure has the highest CO_2 selectivity (fig. S36). Projected crystal orbital Hamiltonian population (pCOHP) analysis was also performed to study the bonding-antibonding characteristics of the metal-adsorbate bond. As shown in Fig. 5 (G to J), negative pCOHP (red) indicates bonding contribution, and positive pCOHP (blue) indicates antibonding contribution. The adsorption of *COOH is mainly attributed to the hybridization of Ni 3d orbital and C 2p orbital. The atomic distance regulation of Ni site changes the Ni 3d orbital, which greatly affects the binding strength between Ni site and *COOH. The more negative integrated COHP (iCOHP) value of *COOH on Ni_1-NC-0.5 (−2.690 eV) is compared with Ni_1-NC-1.7 (−2.546 eV), Ni_1-NC-1.0 (−2.603 eV), and Ni_1-NC-0.36 (−2.565 eV). The above results also verify that Ni_1-NC-0.5 has stronger Ni—C interaction, which will help improve the CO_2RR activity and stability under acidic medium.

Establishment and performance of acidic-alkaline tandem CO_2RR system

To stably and efficiently produce multicarbon products, we established an acidic-alkaline tandem CO_2 electrolysis system by coupling the acidic CO_2-to-CO with the alkaline CO-to-C_2H_4 (Fig. 6A and figs. S37 and S38). We used Ni_1-NC-0.5 for acidic CO_2RR in the first step and the microenvironment-regulated 7,7,8,8-tetracyanoquinolinodimethane (TCNQ)–coated CuO catalyst (CuO@TCNQ; for the specific synthesis process, please refer to the method description section and fig. S39) for CORR in the second step. To match the CO generation rate in CO_2 electrolysis and the CO consumption rate in CO electrolysis, we scaled up the acidic slim flow cell with an effective area of 100 cm^2, and the CO_2 flow rate was set to 300 ml min^{-1}. A three-chamber slim flow cell was used for the acidic CO_2RR to CO process. A 1-mm-thick polyetheretherketone (PEEK) frame was used to form the middle liquid flow channel for the 3 M KCl (pH = 1) catholyte, effectively separating the cathode from the cation exchange membrane (CEM). To minimize the internal ohmic resistance, we tightly hot pressed the CEM and the anode GDE together. The electrolyzer achieved a low resistance of 0.35 ± 0.04 ohms. Acidic CO_2 electrolysis was carried out at a total current of 5 to 50 A (0.05 to 0.5 A cm^{-2}). A low-potential hydrogen oxidation reaction (HOR; H_2-$2e^- = 2H^+$; 0 V versus RHE) was used at the anode instead of the oxygen evolution reaction (OER; 1.23 V versus RHE) to reduce the total overpotential of the electrolyzer and avoid the production of harmful hydrogen peroxide that poisons the CEM (*47*, *48*). Operating under room temperature and pressure conditions helps to reduce the permeation of H_2 through the CEM. CO FE is higher than ~97% at applied current of 5 to 35 A (0.05 to 0.35 A cm^{-2}) (Fig. 6B). The CO FE is 98.4 ± 0.37% at a current density of 0.3 A cm^{-2}, and the cell potential was only 2.85 ± 0.15 V. A CO FE of 90.23 ± 0.98% and a CO formation rate of 18.9 ± 0.2 liters $hour^{-1}$ are achieved at a current density of up to at 0.5 A cm^{-2}. Moreover, the acidic slim flow cell achieves a low cell potential of 3.49 ± 0.1 V and a low power consumption of 0.21 ± 0.01 kWh mol^{-1} at 0.5 A cm^{-2} (Fig. 6C), which is 22.9% lower in cell potential and 22.2% lower in energy consumption than the electrolyzer using OER at the anode (4.53 ± 0.07 V and 0.27 ± 0.001 kWh mol^{-1}; fig. S40). Figure S41 shows that the SPCE of CO_2 reaches 77.2% at the highest level when the flow rate is 50 SCCM. The outlet of the acidic electrolyzer was connected to the CO_2 capture solution and then to the alkaline membrane electrode assembly (MEA) electrolyzer (25 cm^2). To reduce the battery potential and energy consumption of the alkaline MEA, the anode used a hydrazine oxidation reaction (HzOR; $N_2H_4 + 4OH^- = N_2 + 4H_2O$; −0.33 V versus RHE) instead of OER. When a current density of 0.3 A cm^{-2} is applied to the acidic slim flow cell, the alkaline MEA reaches the highest C_2H_4 and C_{2+} FE at current density of 0.4 A cm^{-2}, which were 75.3 ± 1.2 and 92.5 ± 1.3%, respectively (Fig. 6D). At the same time, at current density of 0.4 and 0.48 A cm^{-2}, the C_2H_4 formation rate reaches 851.3 ± 13.2 and 741.5 ± 29.3 ml min^{-1}, respectively. Furthermore, the alkaline MEA achieves a low cell potential of 2.88 ± 0.1 V and a low power consumption of 1.1 ± 0.1 kWh mol^{-1} at 0.48 A cm^{-2} (Fig. 6E), which is 24.4% lower in potential and 26.7% lower in energy consumption than the electrolyzer using OER at the anode (3.81 ± 0.01 V and 1.5 ± 0.05 kWh mol^{-1}) (fig. S42). The highest SPCE of CO to C_2H_4 was measured to be 73.8% at a flow rate of 70 ml min^{-1} (fig. S43).

On the basis of the measured performance of the acidic-alkaline tandem CO_2RR system, we conducted TEA to evaluate the economic feasibility of the system on an industrial manufacturing scale. We first considered the additional cost of using extra hydrogen. The acidic CO_2RR component costs for C_2H_4 production from green hydrogen, blue hydrogen, and gray hydrogen add $357.1/tonne, $214.3/tonne, and $71.4/tonne, respectively (fig. S44). The future use of large-scale green hydrogen for CO_2 conversion is economically feasible. Figure 6F shows that the total cost of C_2H_4 produced using this system is $2219.8/ton at an electricity price of $0.03/kWh, which is close to the commercial price of oil-driven C_2H_4. In addition, the cost breakdown shows that the cost of acidic CO_2RR to CO accounts for 35.5% of the total cost, while alkaline CORR accounts for 64.5%, and electricity costs are still the main cost source for both ($788.7/ton and $1431.0/ton, respectively). These results show that by optimizing the alkaline CORR electrolyzer to reduce the overpotential and designing a more efficient C_2H_4 production catalyst to improve the C_2H_4 selectivity, the cost will be further reduced and lastly form the market competitiveness of C_2H_4 produced by the existing industrial system. On the basis of the further development of power generation technologies (wind power and hydropower, etc.) in the future, when the electricity price drops to $0.01/kWh, the cost of C_2H_4 in this system will decrease to $1343.7/ton, which is expected to replace the high-energy–consuming C_2H_4 production process in traditional petrochemical industries (Fig. 6G). To further prove the industrialization potential of the acid-alkaline tandem CO_2RR system, we conducted a stability test (Fig. 6H). When 20 A (0.2 A cm^{-2}) and 4 A (0.16 A cm^{-2}) are applied to the acidic CO_2RR electrolyzer and alkaline CORR electrolyzer, respectively, the system achieves more than 400 hours of durable operation, and the FE of C_2H_4 is stable at 57.6 ± 2.1%. No carbonate precipitation was observed in the photos of the back of the GDE at different times, indicating that our tandem system effectively alleviates the carbonate problem and improves the stability of C_{2+} preparation. After stability testing, the catalysts at the anode and cathode of the acid-base

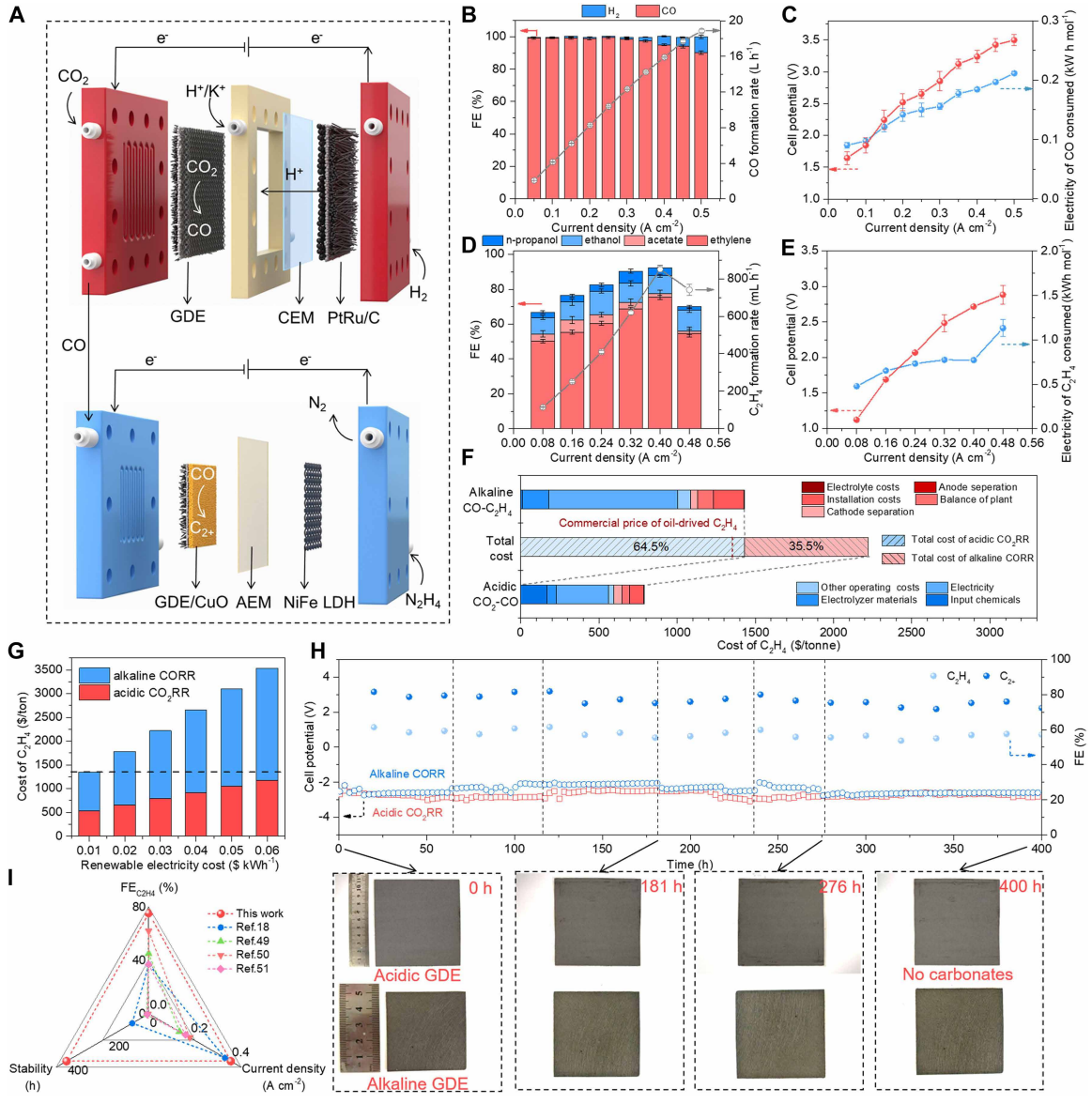

Fig. 6. Detailed illustration and the performance of acidic-alkaline tandem CO_2RR system. (**A**) Schematic of acidic-alkaline tandem CO_2RR system. (**B**) The FE of CO and H_2 and CO product formation rate at different current density in an acidic slim flow cell. (**C**) The cell potential and CO consumed electricity at different current density. (**D**) The FE of C_{2+} products and C_2H_4 product formation rate at different current density in an alkaline MEA. (**E**) The cell potential and C_2H_4 consumed electricity at different current density. (**F**) The TEA of acidic-alkaline tandem CO_2RR system based on this work. The red dashed line shows the current cost of C_2H_4. (**G**) The change of C_2H_4 cost with electricity price. The black dashed line shows the cost of commercial C_2H_4. (**H**) The stability of acidic-alkaline tandem CO_2RR system and digital images of GDEs at different times. The vertical dashed line marks the time of refreshing the electrolyte. (**I**) Comparison of CO_2RR current density, C_2H_4 product FE, and stability of acidic-alkaline tandem CO_2RR system with single-step acidic CO_2RR to C_2H_4.

tandem system were characterized separately. The XRD pattern (fig. S45A) and AC-HAADF-STEM (fig. S45B) results show that the Ni_1-NC-0.5 catalyst maintained single-atom dispersion without agglomeration, with only 4.69% Ni loading lost to the cathode electrolyte (fig. S45C). CuO@TCNQ experiences only a 0.85% Cu loss during the CORR process (fig. S45D). CuO@TCNQ was reduced to Cu^0 after the reaction but still retained its nanosheet morphology (fig. S46). Furthermore, in situ Raman spectroscopy revealed that the characteristic vibrational peak of Cu—O at ~303 cm^{-1} gradually weakened and completely disappeared at 130 min (0.16 A cm^{-2}) and 100 min (0.4 A cm^{-2}), respectively (fig. S47). This indicates that the Cu^0 structure obtained by the gradual reduction of CuO to its valence state during the CORR is the true active site. Ex situ XRD, HAADF-STEM, and scanning electron microscope (SEM) analyses show no notable changes in the anode catalysts [PtRu black and NiFe–layered double hydroxides (LDHs)] after the reaction (figs. S48 and S49), indicating that the structure and morphology of the anode catalysts remained stable (detailed analysis results are provided in the Supplementary Materials). To demonstrate its industrial potential, we subjected the acidic CO_2 reduction electrolyzer and the alkaline CO_2 reduction electrolyzer to currents of 40 A (0.4 A cm^{-2}) and 10 A (0.4 A cm^{-2}), respectively. The system achieved stable operation

for more than 100 hours, with the FE of C2H4 maintained at a stable level of 70.2 ± 2.5% (fig. S50). The loss of both Ni and Cu decreased after stability testing at higher overpotentials, which also indicates the stability of the cathode catalyst in the acidic-alkaline tandem system (fig. S51). Figure 6I compares the current density, FE, and stability of the acidic CO_2RR directly preparing C_2H_4 reported previously (*23*, *49*–*51*). The stability and activity of the acidic-alkaline tandem CO_2 electrolysis are superior to those of the previously reported single-step direct electrolysis and alkaline-alkaline tandem electrolysis systems (table S14). The acidic-alkaline tandem CO_2RR system provides guidance for the stable preparation of C_{2+} products such as CO_2 to C_2H_4.

DISCUSSION

In conclusion, we achieve enhanced acidic CO_2RR by controlling the site distance and established a highly durable acidic-alkaline tandem system to convert CO_2-to-C_{2+}. For Ni sites with a 0.5-nm distance and a current density of 1.4 A cm^{-2}, nearly 100% CO FE is achieved at pH = 1. Further coupling with alkaline CORR enables the durable production of C_{2+}, especially C_2H_4 at industrial current for more than 400 hours. The acidic-alkaline tandem CO_2RR system has proven to be an effective solution for CO_2 conversion, providing a reference for future industrial-scale electrochemical production of C_2H_4.

MATERIALS AND METHODS

Materials and chemicals

DCD (>99%), HCHO (37 wt % solution), ferric nitrate nonahydrate [$Fe(NO_3)_3{\cdot}9H_2O$; >99%], cobaltous nitrate hexahydrate [$Co(NO_3)_2{\cdot}6H_2O$; >99%], nickel nitrate hexahydrate [$Ni(NO_3)_2{\cdot}6H_2O$; >99%], copper nitrate trihydrate [$Cu(NO_3)_2{\cdot}3H_2O$; >99%], zinc nitrate hexahydrate [$Zn(NO_3)_2{\cdot}6H_2O$; >99%], potassium hydroxide (KOH; >85%), and hydrazine hydrate ($N_2H_4{\cdot}H_2O$) were purchased from Sinopharm Chemical Reagent Co. Ltd. (China). SiO_2 (~20 nm) was purchased from XFNANO. Iridium (III) chloride hydrate ($IrCl_3{\cdot}xH_2O$; 99.9%) was purchased from Alfa Aesar. TCNQ (>99%) was purchased from Sigma-Aldrich. All of the chemicals used in this experiment were analytical grade and used without further purification. Deionized (DI) water from a Milli-Q System (Millipore, Billerica, MA, USA) was used in all experiments.

Ni_1-NC-X synthesis

The Ni_1-NC-X catalyst was fabricated through a coordinated polymer pyrolysis strategy. A total of 2 g of SiO_2, 5 g of DCD, and the corresponding mass of $Ni(NO_3)_2{\cdot}6H_2O$ was mixed in 20 ml of DI water and then stirred at 60°C until DCD was completely dissolved. Then, 4.4 ml of HCHO was added and heated for 6 hours until water was completely evaporated to obtain an orange solid. In this process, HCHO and DCD polymerized; Ni ions thoroughly coordinated with DCD-HCHO resin. The solid was next placed in a quartz boat and heated to 900°C in a tube furnace for 2 hours under Ar atmosphere. After cooling to room temperature, the black solid was etched with HF to remove SiO_2, then centrifuged, washed three times each with water and ethanol, and vacuum dried overnight to obtain Ni_1-NC-X catalyst. For Ni_1-NC-1.7, Ni_1-NC-1.0, Ni_1-NC-0.5, and Ni_1-NC-0.36, the masses of $Ni(NO_3)_2{\cdot}6H_2O$ added were 50, 150, 280, and 360 mg, respectively, and other conditions remained the same. For Fe_1-NC-X, Co_1-NC-X, Cu_1-NC-X, and Zn_1-NC-X, the masses of the corresponding metal nitrates are shown in table S10, and the other conditions remain the same.

CuO@TCNQ synthesis

CuO@TCNQ was prepared by an improved method (*52*). First, CuO nanosheets were synthesized by a hydrothermal method. In a typical experiment, 0.5 g of $CuCl_2$ was dissolved in 30 ml of water. Then, 30 ml of 3 M NaOH solution was added dropwise. The resulting mixture was stirred for 20 min, and 20 ml ethanol was then added. The obtained mixture was transferred into a Teflon-lined stainless steel autoclave and was heated at 100°C under autogenous pressure for 10 hours. The resulting solids were collected by centrifugation, washed with DI water, and dried at 60°C overnight in a vacuum oven. To prepare the TCNQ/acetonitrile solution, TCNQ was dissolved in acetonitrile at a concentration of 10 mM. Next, 30 mg of CuO powder was dispersed in 4 ml of methanol. Then, 150 μl of TCNQ/acetonitrile was added to the above mixture under ultrasonication for 1 hour, after which 150 μl of Nafion was added, and the mixture was ultrasonicated for another 1 hour to prepare the ink. The resulting suspension was spray coated onto a 5 cm–by–5 cm YLS-30T carbon paper to prepare the CuO@TCNQ electrode with a loading amount of about 1 mg cm^{-2}.

Characterization

Powder XRD patterns of samples were recorded on a Rigaku MiniFlex 600 operating at a 40-kV voltage and a 15-mA current with Cu Kα radiation (λ =0.15406 nm). AC-HAADF-STEM imaging and EELS of samples were performed on a JEM-ARM200F. High-resolution transmission electron microscope were performed on a Talos F200X at 200 kV and Themis Z at 300 kV. SEM was performed on a Gemini SEM 500. The XPS was recorded on a Thermo Fisher Scientific Nexsa G2 spectrometer with an excitation source of monochromatized Al Ka ($h\nu$ = 1486.6 eV) and a pass energy of 40 eV. XAFS spectroscopy measurements were performed at the Ni K-edge. Data were collected at the 1W1B station in Beijing Synchrotron Radiation Facility (BSRF) and BL14W1 in the Shanghai Synchrotron Radiation Facility (SSRF), China. Ni foil was used as references. The Ni K-edge XANES data were recorded in a transmission/fluorescence mode using N_2-filled ionization chamber. The storage ring was working at the energy of 3.5 GeV with an average electron current of 250 mA. All samples were pelletized as disks of 13-mm diameter using graphite powder as a binder. The Brunauer-Emmett-Teller test was obtained from Micromeritics ASAP 2020 HD88 Plus. All the samples were degassed at 573 K for 3 hours. The pore size distribution was calculated from the Horvath-Kawazoe and Barrett–Joyner–Halenda method for micropore and mesoporous, respectively. The EPR spectra were recorded on a JEOL JES-FA200 EPR spectrometer. Contact angles of CO_2 and H_2O were measured using Lauda Scientific LSA 100. Raman spectral analysis was carried out with a HORIBA LabRAM HR Raman spectrometer with a wavelength of 785 nm. The FTIR spectra were collected at a resolution of 4 cm^{-1} on a Bruker INVENIO spectrophotometer. The liquid products were quantified by nuclear magnetic resonance (NMR) (Bruker Avance AV III 400) spectroscopy using dimethyl sulfoxide as an internal standard. During chronoamperometry, the effluent gas from the cell went through the sampling loop of a gas chromatograph (Panna A91) and was

analyzed to determine the concentration of gas products. The gas chromatograph was equipped with a molecular sieve 5A, Porapak Q 80/100 mesh, SE-30, and HP-Al_2O_3/S capillary column with ultra-high purity helium as a carrier gas.

CO_2 electrolysis measurements

Preparation of GDEs

Typically, 14 mg of catalyst was mixed with 70 μl of 5 wt % Nafion solution and 2 ml of ethanol. The solution was sonicated for at least 60 min at room temperature. The well-dispersed ink was then air-brushed onto YLS-30T or Sigracet 28 BC (3 cm by 4 cm) using an Anest Iwata RG-3L airbrush (Japan) pumped by an air compressor at a fixed pressure of 0.4 MPa. The GDEs were cut to 3.0 cm by 1.0 cm and dried in a vacuum chamber overnight before use. The loading amount was determined by weighing the GDEs before and after the airbrushing and was found to be roughly 1.0 mg cm^{-2}. For large-area GDEs (11 cm by 11 cm and 5 cm by 5 cm), the well-dispersed ink was then airbrushed onto a carbon paper by an ultrasonic spray pyrolysis system flux spray machine (UAM4000L, Cheersonic Ultrasonics Equipment, China). The loading amount was also estimated to be 1.0 mg cm^{-2}.

Preparation of the anode IrO_2-Ti mesh

The anodes were prepared by a modified dip coating and thermal decomposition method by depositing IrO_2 on a titanium mesh (*1*). Briefly, the titanium mesh was first degreased with acetone and DI water and then etched in a 6 M HCl solution 20 min before dip coating. The dip coating solution consisted of 30 mg of $IrCl_3{\cdot}xH_2O$ (Alfa Aesar) dissolved in 9 ml of isopropanol and 1 ml of concentrated HCl. Subsequently, the etched titanium mesh was dipped into the $IrCl_3$ solution and dried under a heat lamp before calcination in a furnace at 500°C for 10 min. The dipping and calcination process was repeated until a suitable loading was achieved (2 mg cm^{-2}), and then the IrO_2-Ti mesh was used in flow cell (1 cm by 3 cm) and slim flow cell (11 cm by 11 cm) for acidic CO_2RR system.

Preparation of the anode NiFe-LDHs/Ni foam

The anodes were prepared by an electrodeposition method by depositing NiFe-LDHs on a Ni foam (*53*). Before synthesis, Ni foam was ultrasonicated in 5 M HCl aqueous solution for 2 min and then washed by DI water and absolute ethanol repeatedly, followed by drying in a vacuum oven at 60°C. The NiFe-LDHs was electrodeposited on the as-prepared Ni foam in 250 ml of electrolyte bath containing $Ni(NO_3)_2{\cdot}6H_2O$ (3 mM) and $Fe(NO_3)_3{\cdot}9H_2O$ (3 mM) at −1.0 V (versus Ag/AgCl) at 25°C for 480 s. Eventually, the self-supported flexible NiFe-LDHs on Ni foam electrocatalyst was obtained for OER and HzOR. After reaction, the NiFe-LDHs/Ni foam was rinsed thoroughly with DI water and dried at room temperature. The NiFe-LDHs/Ni foam anode was used in the alkaline CORR system.

Acidic CO_2 electrolysis in a flow cell

The gas-tight flow cell system was fabricated with a CO_2 gas compartment and two liquid compartments with channels of dimensions 1.0 cm by 3.0 cm by 0.3 cm. A total of 3 M KCl (use H_2SO_4 to adjust the pH to 1) aqueous solution was pumped at 20 ml min^{-1} as cathode electrolyte. The CO_2 flow rate is controlled at 40 ml min^{-1} using a mass flow meter, and the flow rate at the outlet is corrected using a soap film flow meter. IrO_2-Ti mesh and 0.5 M H_2SO_4 were used for the anodic OER. The catholyte and anolyte were separated by a CEM (Nafion 212, Dioxide Materials). The electrolysis was carried out in the galvanostatic mode using a CHI 1140C. All potentials were measured against a Ag/AgCl reference electrode (saturated KCl, obtained from Tjaida and stored in a saturated KCl solution before use) and converted to the RHE scale by

$$E_{\mathrm{VS.RHE}} = \mathrm{E}_{\mathrm{VS.Ag/AgCl}} + 0.22\ \mathrm{V} + 0.059 \times \mathrm{pH} \quad (1)$$

The corrected potential at the cathode is given by

$$E_{\mathrm{VS.Ag/AgCl}} = \mathrm{E} - 0.85 \times I_{\mathrm{tot}} \times R \quad (2)$$

where I_{tot} is the total current through the cell (in amperes). A factor of 0.85 is applied for the ohmic potential drop. $R = 0.8$ ohms for the flow cell.

Acidic-alkaline tandem CO_2RR system

CO_2RR performance measurements for tandem system were conducted in slim flow cell and MEA-based electrolyzer. The titanium plates are used for the cathode and anode for current collecting. For acidic slim flow cell, at the cathode compartment, a GDE (11 cm by 11 cm) was used for CO_2 supplying, IrO_2-Ti mesh anode and 0.5 M H_2SO_4 were used for OER, platinum-ruthenium black (Sinero, SP-T65RU35) GDEs anode and H_2 were used for HOR. The cathode and anode were separated by a Nafion 212. Hot pressing is conducted at 60°C and 1 MPa to ensure a tight bond between the CEM and GDE, thereby reducing resistance. Acidic CO_2RR performance was measured using chronopotentionmetry in the galvanostatic mode by a Henghui potentiostat/galvanostat (HCP1023C). Pure CO_2 was fed into the cathode at a flow rate of 300 ml min^{-1}, while 3 M KCl aqueous solution (use H_2SO_4 to adjust the pH to 1) at a flow rate of 50 ml min^{-1} was fed into the cathode. The H_2 flow rate at the anode was set to 50 ml min^{-1}. The outlet gas is fed with concentrated NaOH to trap CO_2. For alkaline MEA, at the cathode compartment, a GDE (5 cm by 5 cm) was used for CO supplying. NiFe-LDH anode and 1 M KOH or 1 M KOH/0.4 M N_2H_4 were used for OER or hydrazine oxidation. The cathode and anode were separated by an anion exchange membrane (Sustainion X37-50 RT, Dioxide Materials). Alkaline CORR performance was measured using chronopotentionmetry in the galvanostatic mode by a Henghui potentiostat/galvanostat (HCP1023C). During the stability testing process, the electrolysis procedure is periodically paused. The fresh electrolyte and NaOH capture solution are replaced. The cathode's GDE is rinsed several times with DI water and then dried in a vacuum oven to remove residual carbonates and moisture from the flow channels. Subsequently, a diluted polytetrafluoroethylene dispersion is applied to the backside of the GDE to restore its hydrophobic properties.

Product analysis

Gas products were analyzed by a thermal conductivity detector (for H_2 and CO) and a flame ionization detector (for alkanes and alkenes). Quantification of the products was performed using standard calibration gasses. Liquid products were analyzed by quantitative ^{1}H NMR spectroscopy with water suppression and using dimethyl sulfoxide as an internal standard. For each data point, the electrolyzer was allowed to reach a steady state, and the products were quantified over periods of 30-min periods. A new GDE was used every time a galvanostatic test is performed. To ensure accuracy, at least three measurements were performed and averaged at each current density.

The *FE* is calculated as Eqs. 3 and 4

$$FE_{\mathrm{gas}} = \frac{x_i \times v \times P_0 \times z_i \times F}{R \times T \times I_{\mathrm{total}}} \times 100\,\% \quad (3)$$

$$FE_{\mathrm{liquid}} = \frac{n_i \times z_i \times F}{\Delta t \times I_{\mathrm{total}}} \times 100\,\% \quad (4)$$

respectively, where x_i is the volume fraction of gas product *i*, *v* is the gas flow rate at the cathode outlet, z_i is the number of electrons involved in the reaction to produce one molecule of product *i*, *F* is the Faradaic constant (in coulombs per mole), P_0 is the absolute pressure (101.325 kPa), *R* is the gas constant, *T* is the temperature (in kelvin), I_{tot} is the total current, and n_i the number of moles of product *i* per time Δt (in seconds).

The TOF is calculated as Eq. 5

$$TOF_{CO} = \frac{I_{product}/(n \times F)}{m \times \omega/M} \times t \quad (5)$$

where $I_{product}$ is the partial current of CO product (in amperes), *n* is the electron transfer for the formation of each CO molecule, *F* is the Faradaic constant (in coulombs per mole), *m* is catalyst mass in the GDEs (in grams), ω is the active metal loading in the catalyst, *M* is atomic mass of active metal, and *t* is 3600 s.

The half-cell ECE for CO product is calculated as Eq. 6

$$\text{Half} - \text{cell } ECE_{CO} = \frac{(E_{anode} - E_{CO}) \times FE_{CO}}{1.23 - E_{app}} \quad (6)$$

where E_{anode} is the thermodynamic potential (versus RHE) for anode reaction, which is 1.23 V for OER. E_{CO} is the thermodynamic potential (versus RHE) for CO_2RR to CO, which is 0.109 V. E_{app} is the applied potential (versus RHE) in three-electrode setup. The CO_2 SPCE toward CO or C_2H_4 product is determined using the following Eq. 7 at 25°C and 1 atm

$$SPCE = \frac{(I_{product} \times 60\ s)/(n \times F)}{(v \times 1\ min) \times V_m} \quad (7)$$

where $I_{product}$ is the partial current of CO or C_2H_4 product (in amperes), *n* is the electron transfer for the formation of each product molecule, *F* is the Faradaic constant (in coulombs per mole), and $V_m = 24.5$ liters mol^{-1}. The formation rate (*R*) for CO and C_2H_4 is calculated using the following Eq. 8

$$R = \frac{q_{tot} \times FE}{96{,}485 \times z \times t \times S} \quad (8)$$

where q_{tot} is the total charge passed toward CO or C_2H_4 products (in coulombs), *FE* is Faradaic efficiency for CO or C_2H_4 product (%), *z* is the number of electrons involved in the reaction to produce one molecule of CO or C_2H_4 product, *t* is the electrolysis time (in hours), and *S* is the geometric area of the electrode (in square centimeters).

The consumed electricity (CE) for CO or C_2H_4 is calculated using the following Eq. 9

$$CE = \frac{E \times z \times F}{FE \times t} \quad (9)$$

where *E* is the cell potential (in volts), *z* is the number of electrons involved in the reaction to produce one molecule of CO or C_2H_4 product, *F* is the Faradaic constant (in coulombs per mole), *FE* is Faradaic efficiency for CO or C_2H_4 product (%), and *t* was the electrolysis time (hours).

In situ physicochemical characterizations

In situ SERS

The in situ SERS measurements were performed in a flow cell with a three-electrode configuration, where a GDE, a graphite rod, and a Ag/AgCl electrode were used as the cathode, anode, and reference electrode, respectively. A piece of anion exchange membrane was used to separate the cathode chamber from the anode chamber. A total of 3 M KCl (use H_2SO_4 to adjust the pH to 1) was circulated through the cathode chamber by a peristaltic pump at a flow rate of 5 ml min^{-1}, and CO_2 gas was passed through the back side of the GDE during experiments. Raman spectra were collected with a Raman spectrometer (HORIBA LabRAM HR) with a 785-nm excitation laser. A monocrystalline silicon wafer standard (520.7 cm^{-1}) was used for calibration before Raman measurements. Spectral signals were collected after stable electrolysis at each potential. Under each potential, the collection time of each Raman spectrum was set as 30 s.

In situ ATR surface-enhanced infrared absorption spectroscopy

A spectroelectrochemical H-cell with a three-electrode configuration (Beijing SciStar Co. Ltd.) was used for in situ ATR–surface-enhanced infrared absorption spectroscopy (SEIRAS) tests, where the as-prepared electrodes, a Pt wire, and a Ag/AgCl electrode were used as working electrodes, counter electrode, and reference electrode, respectively. The silicon crystal is deposited by ion sputtering at a current of 30 mA for 6 min to achieve uniform coverage of the gold film on the surface. The cell was integrated into a Bruker INVENIO FTIR spectrometer equipped with a liquid nitrogen–cooled MCT detector. A total of 0.5 M $KHCO_3$ solution in D_2O was used as electrolyte bubbled with CO_2 at a flow rate of 20 ml min^{-1}. Each spectrum consisted of 32 single beams with a resolution of 4 cm^{-1}. The spectrum collected at OCP in CO_2-saturated 0.5 M $KHCO_3$ was used as a background. Spectral signals were collected after stable electrolysis at each potential.

In situ XAS

The in situ XAS of the Ni_1-NC-X was acquired in the as-prepared state and under CO_2RR conditions at different potential using a homemade flow cell with an IrO_2-Ti mesh counter electrode and a Ag/AgCl reference electrode. A total of 3 M KCl (use H_2SO_4 to adjust the pH to 1) was used as electrolyte with CO_2 at a flow rate of 20 ml min^{-1}. After each potential was run for 20 min, signal acquisition began. The XAS spectra at Ni K edge ($E_0 = 8333$ eV) were performed at beamline 1W2B at BSRF. The data were obtained using fluorescence-yield mode and taking metallic Ni foil as a reference to calibrate the energy scale. The data were processed using IFEFFIT package including ATHENA and ARTEMIS. The XAS data were processed by baseline subtracting and normalizing, noting as "normalized absorbance." The Fourier transformed EXAFS data were fitted by applying metallic NiO model for Ni-O contributions. CN, interatomic distances (*R*), Debye-Waller factors (σ^2), and energy shift (ΔE) were the fitting results.

DFT calculations

The Vienna Ab initio Simulation Package (VASP) was used for all DFT calculations (*54*). Spin-polarized implementations adopted the generalized gradient approximation framework with the Perdew-Burke-Ernzerhof functional governing exchange-correlation interactions (*55*). Ion-electron dynamics were described through the projector augmented-wave method (*56*). The Gaussian smearing

method was used with a plane wave cutoff energy of 420 eV, and the calculations were continued until the total energy converged to 10^{-5} eV. The force convergence criterion was set at 0.01 eV/Å. The implicit solvation model implemented by VASPsol (*57*) is also used to treat the aqueous environment of the electrolyte, and the dielectric constant of the aqueous solvent is set to 78.4. The Brillouin zone was sampled with 3 × 3 × 1 during the calculations. A vacuum layer of 15 Å was introduced to prevent interactions between periodic slabs. According to the computational hydrogen electrode model proposed by Nørskov *et al.* (*58*), the changes in Gibbs free energy were computed as $\Delta G = \Delta E + \Delta \mathrm{ZPE} - T\Delta S + \Delta G_U + \Delta G_{\mathrm{pH}}$, Here, where ΔE denotes the electronic energy difference determined by DFT, $\Delta \mathrm{ZPE}$ and ΔS represent the changes in zero-point energy and entropy at 298.15 K, respectively. ΔG_U is the contribution of the applied electrode potential, and ΔG_{pH} indicates the energy impact of pH. In this study, the pH was set to 0. The bonding interactions between catalytic sites and intermediates were quantified through crystal orbital Hamiltonian Population (COHP) and integrated COHP (iCOHP) values calculated using LOBSTER 4.1.0 (*59*, *60*).

Supplementary Materials

This PDF file includes:

Figs. S1 to S51
Supplementary Text
Tables S1 to S14
References

REFERENCES

1. C. Gabardo, C. Brien, J. Edwards, C. McCallum, Y. Xu, C. Dinh, J. Li, E. Sargent, D. Sinton, Continuous carbon dioxide electroreduction to concentrated multi-carbon products using a membrane electrode assembly. *Joule* **3**, 2777–2791 (2019).
2. J. Kim, C. Sellers, S. Hao, T. Senftle, H. Wang, Different distributions of multi-carbon products in CO_2 and CO electroreduction under practical reaction conditions. *Nat. Catal.* **6**, 1115–1124 (2023).
3. D. Gao, R. Arán-Ais, H. Jeon, B. Cuenya, Rational catalyst and electrolyte design for CO_2 electroreduction towards multicarbon products. *Nat. Catal.* **2**, 198–210 (2019).
4. W. Ma, X. He, W. Wang, S. Xie, Q. Zhang, Y. Wang, Electrocatalytic reduction of CO_2 and CO to multi-carbon compounds over Cu-based catalysts. *Chem. Soc. Rev.* **50**, 12897–12914 (2021).
5. G. Wu, Y. Song, Q. Zheng, C. Long, T. Fan, Z. Yang, X. Huang, Q. Li, Y. Sun, L. Zuo, S. Lei, Z. Tang, Selective electroreduction of CO_2 to *n*-propanol in two-step tandem catalytic system. *Adv. Energy Mater.* **12**, 2202054 (2022).
6. T. Möller, M. Filippi, S. Brückner, W. Ju, P. Strasser, A CO_2 electrolyzer tandem cell system for CO_2-CO co-feed valorization in a Ni-N-C/Cu-catalyzed reaction cascade. *Nat. Commun.* **14**, 5680 (2023).
7. B. S. Crandall, B. H. Ko, S. Overa, L. Cherniack, A. Lee, I. Minnie, F. Jiao, Kilowatt-scale tandem CO_2 electrolysis for enhanced acetate and ethylene production. *Nat. Chem. Eng.* **1**, 421–429 (2024).
8. S. Garg, Z. Xie, J. G. Chen, Tandem reactors and reactions for CO_2 conversion. *Nat. Chem. Eng.* **1**, 139–148 (2024).
9. Y. Ji, A. Guan, G. Zheng, Copper-based catalysts for electrochemical carbon monoxide reduction. *Cell Rep. Phys. Sci.* **3**, 101072 (2022).
10. M. Jouny, G. S. Hutchings, F. Jiao, Carbon monoxide electroreduction as an emerging platform for carbon utilization. *Nat. Catal.* **2**, 1062–1070 (2019).
11. X. Wang, Y. Chen, F. Li, R. Kai Miao, J. E. Huang, Z. Zhao, X. Li, R. Dorakhan, S. Chu, J. Wu, S. Zheng, W. Ni, D. Kim, S. Park, Y. Liang, A. Ozden, P. Ou, Y. Hou, D. Sinton, E. H. Sargent, Site-selective protonation enables efficient carbon monoxide electroreduction to acetate. *Nat. Commun.* **15**, 616 (2024).
12. Y. Xu, Z. Xia, W. Gao, H. Xiao, B. Xu, Cation effect on the elementary steps of the electrochemical CO reduction reaction on Cu. *Nat. Catal.* **7**, 1120–1129 (2024).
13. Y. Xie, P. Ou, X. Wang, Z. Xu, Y. C. Li, Z. Wang, J. E. Huang, J. Wicks, C. McCallum, N. Wang, Y. Wang, T. Chen, B. T. W. Lo, D. Sinton, J. C. Yu, Y. Wang, E. H. Sargent, High carbon utilization in CO_2 reduction to multi-carbon products in acidic media. *Nat. Catal.* **5**, 564–570 (2022).
14. X. Ma, T. Yang, D. He, X. Gao, W. Jiang, D. Li, Y. Sun, X. Lin, J. Xu, H. Wang, X. Tai, Y. Lin, T. Yao, H. Zhou, Y. Wu, Carbonate shell regulates CuO surface reconstruction for enhanced CO_2 electroreduction. *Nat. Synth.* **4**, 53–66 (2025).
15. K. Yang, R. Kas, W. A. Smith, T. Burdyny, Role of the carbon-based gas diffusion layer on flooding in a gas diffusion electrode cell for electrochemical CO_2 reduction. *ACS Energy Lett.* **6**, 33–40 (2021).
16. M. Sassenburg, M. Kelly, S. Subramanian, W. A. Smith, T. Burdyny, Zero-gap electrochemical CO_2 reduction cells: Challenges and operational strategies for prevention of salt precipitation. *ACS Energy Lett.* **8**, 321–331 (2023).
17. S. Hao, A. Elgazzar, N. Ravi, T. Wi, P. Zhu, Y. Feng, Y. Xia, F. Chen, X. Shan, H. Wang, Improving the operational stability of electrochemical CO_2 reduction reaction via salt precipitation understanding and management. *Nat. Energy* **10**, 266–277 (2025).
18. J. Gu, S. Liu, W. Ni, W. Ren, S. Haussener, X. Hu, Modulating electric field distribution by alkali cations for CO_2 electroreduction in strongly acidic medium. *Nat. Catal.* **5**, 268–276 (2022).
19. J. E. Huang, F. Li, A. Ozden, A. S. Rasouli, F. P. G. de Arquer, S. Liu, S. Zhang, M. Luo, X. Wang, Y. Lum, Y. Xu, K. Bertens, R. Miao, C. Dinh, D. Sinton, E. H. Sargent, CO_2 electrolysis to multicarbon products in strong acid. *Science* **372**, 1074–1078 (2021).
20. W. Lai, Y. Qiao, Y. Wang, H. Huang, Stability issues in electrochemical CO_2 reduction: Recent advances in fundamental understanding and design strategies. *Adv. Mater.* **35**, e2306288 (2023).
21. N. Dutta, S. C. Peter, Electrochemical CO_2 reduction in acidic media: A perspective. *J. Am. Chem. Soc.* **147**, 9019–9036 (2025).
22. M. Zeng, W. Fang, Y. Cen, X. Zhang, Y. Hu, B. Xia, Reaction environment regulation for electrocatalytic CO_2 reduction in acids. *Angew. Chem. Int. Ed. Engl.* **63**, e202404574 (2024).
23. Y. Wu, C. Chen, S. Liu, Q. Qian, Q. Zhu, R. Feng, L. Jing, X. Kang, X. Sun, B. Han, Highly selective CO_2 electroreduction to multi-carbon alcohols via amine modified copper nanoparticles at acidic conditions. *Angew. Chem. Int. Ed. Engl.* **63**, e202410659 (2024).
24. B. Zhao, F. Chen, M. Wang, C. Cheng, Y. Wu, C. Liu, Y. Yu, B. Zhang, Economically viable electrocatalytic ethylene production with high yield and selectivity. *Nat. Sustain.* **6**, 827–837 (2023).
25. X. Su, X. Yang, Y. Huang, B. Liu, T. Zhang, Single-atom catalysis toward efficient CO_2 conversion to co and formate products. *Acc. Chem. Res.* **52**, 656–664 (2019).
26. Y. Ji, J. Du, A. Chen, X. Gao, M. Peng, Transition metal-nitrogen-carbon single-atom catalysts enhanced CO_2 electroreduction reaction: A review. *ChemSusChem* **18**, e202401557 (2025).
27. J. Shen, D. Wang, How to select heterogeneous CO_2 reduction electrocatalyst. *Nano Res. Energy* **3**, e9120096 (2024).
28. T. Zheng, K. Jiang, N. Ta, Y. Hu, J. Zeng, J. Liu, H. Wang, Large-scale and highly selective CO_2 electrocatalytic reduction on nickel single-atom catalyst. *Joule* **3**, 265–278 (2019).
29. M. D. Hossain, Y. Huang, T. H. Yu, W. A. Goddard III, Z. Luo, Reaction mechanism and kinetics for CO_2 reduction on nickel single atom catalysts from quantum mechanics. *Nat. Commun.* **11**, 2256 (2020).
30. C. Zhao, X. Dai, T. Yao, W. Chen, X. Wang, J. Wang, J. Yang, S. Wei, Y. Wu, Y. Li, Ionic exchange of metal–organic frameworks to access single nickel sites for efficient electroreduction of CO_2. *J. Am. Chem. Soc.* **139**, 8078–8081 (2017).
31. Z. Zhao, J. Zhang, M. Lei, Y. Lum, Reviewing the impact of halides on electrochemical CO_2 reduction. *Nano Res. Energy* **2**, e9120044 (2023).
32. Y. Qin, W. Zhao, C. Xia, L. Yu, F. Song, J. Zhang, T. Wu, R. Cao, S. Ding, B. Xia, Y. Su, CO intermediate-assisted dynamic Cu sintering during electrocatalytic CO_2 reduction on Cu–N–C catalysts. *Angew. Chem. Int. Ed. Engl.* **63**, e202404763 (2024).
33. J. Yang, H. Qi, A. Li, X. Liu, X. Yang, S. Zhang, Q. Zhao, Q. Jiang, Y. Su, L. Zhang, J. Li, Z. Tian, W. Liu, A. Wang, T. Zhang, Potential-driven restructuring of Cu single atoms to nanoparticles for boosting the electrochemical reduction of nitrate to ammonia. *J. Am. Chem. Soc.* **144**, 12062–12071 (2022).
34. Y. Zeng, J. Zhao, S. Wang, X. Ren, Y. Tan, Y. Lu, S. Xi, J. Wang, F. Jaouen, X. Li, Y. Huang, T. Zhang, B. Liu, Unraveling the electronic structure and dynamics of the atomically dispersed iron sites in electrochemical CO_2 reduction. *J. Am. Chem. Soc.* **145**, 15600–15610 (2023).
35. J. Ding, L. Liu, J. Zhang, Y. Liu, H. Xu, Z. Shen, H. Yang, X. Feng, Y. Huang, B. Liu, Unraveling dynamic structural evolution of single atom catalyst via in situ surface-enhanced infrared absorption spectroscopy. *J. Am. Chem. Soc.* **147**, 9601–9609 (2025).
36. Q. Ruan, S. Lu, J. Wu, Y. Shi, B. Zhang, Structural degradation of M-N-C (M=Co, Ni and Fe) single-atom electrocatalysts at industrial-grade current density for long-term reduction. *Angew. Chem. Int. Ed. Engl.* **63**, e202409000 (2024).
37. Y. Cui, C. Ren, M. Wu, Y. Chen, Q. Li, C. Ling, J. Wang, Structure–stability relation of single-atom catalysts under operating conditions of CO_2 reduction. *J. Am. Chem. Soc.* **146**, 29169–29176 (2024).
38. L. Zhang, J. Feng, S. Liu, X. Tan, L. Wu, S. Jia, L. Xu, X. Ma, X. Song, J. Ma, X. Sun, B. Han, Atomically dispersed Ni–Cu catalysts for pH-universal CO_2 electroreduction. *Adv. Mater.* **35**, e2209590 (2023).

39. H. Li, H. Li, P. Wei, Y. Wang, Y. Zang, D. Gao, G. Wang, X. Bao, Tailoring acidic microenvironments for carbon-efficient CO_2 electrolysis over a Ni–N–C catalyst in a membrane electrode assembly electrolyzer. *Energy Environ. Sci.* **16**, 1502–1510 (2023).
40. Q. Zhang, C. B. Musgrave III, Y. Song, J. Su, L. Huang, L. Cheng, G. Li, Y. Liu, Y. Xin, Q. Hu, G. Ye, H. Shen, X. Wang, B. Tang, W. A. Goddard III, R. Ye, A covalent molecular design enabling efficient CO_2 reduction in strong acids. *Nat. Synth.* **3**, 1231–1242 (2024).
41. K. Jiang, H. Wang, W. Cai, H. Wang, Li electrochemical tuning of metal oxide for highly selective CO_2 reduction. *ACS Nano* **11**, 6451–6458 (2017).
42. N. J. Firet, W. A. Smith, Probing the reaction mechanism of CO_2 electroreduction over Ag films via operando infrared spectroscopy. *ACS Catal.* **7**, 606–612 (2017).
43. Y. Xu, X. Zhang, C. Yang, C. Gong, X. Qin, H. Sun, H. Chen, M. A. Soldatov, K. Zheng, C. Li, T. Gan, J. Li, J. He, Q. Liu, Silver single atoms combined with clusters on carbon nanotubes mediates exclusive electrochemical CO_2-to-CO conversion. *Adv. Energy Mater.* **14**, 2400143 (2024).
44. J. Wang, Y. Huang, Y. Wang, H. Deng, Y. Shi, D. Wei, M. Li, C. Dong, H. Jin, S. S. Mao, S. Shen, Atomically dispersed metal–nitrogen–carbon catalysts with d-orbital electronic configuration-dependent selectivity for electrochemical CO_2-to-CO reduction. *ACS Catal.* **13**, 2374–2385 (2023).
45. F. Wu, X. Liu, S. Wang, L. Hu, S. Kunze, Z. Xue, Z. Shen, Y. Yang, X. Wang, M. Fan, H. Pan, X. Gao, T. Yao, Y. Wu, Identification of K^+-determined reaction pathway for facilitated kinetics of CO_2 electroreduction. *Nat. Commun.* **15**, 6972 (2024).
46. Q. Jia, N. Ramaswamy, H. Hafiz, U. Tylus, K. Strickland, G. Wu, B. Barbiellini, A. Bansil, E. F. Holby, P. Zelenay, S. Mukerjee, Experimental observation of redox-induced Fe–N switching behavior as a determinant role for oxygen reduction activity. *ACS Nano* **9**, 12496–12505 (2015).
47. W. Fang, W. Guo, R. Lu, Y. Yan, X. Liu, D. Wu, F. Li, Y. Zhou, C. He, C. Xia, H. Niu, S. Wang, Y. Liu, Y. Mao, C. Zhang, B. You, Y. Pang, L. Duan, X. Yang, F. Song, T. Zhai, G. Wang, X. Guo, B. Tan, T. Yao, Z. Wang, B. Xia, Durable CO_2 conversion in the proton-exchange membrane system. *Nature* **626**, 86–91 (2024).
48. L. Fan, C. Xia, P. Zhu, Y. Lu, H. Wang, Electrochemical CO_2 reduction to high-concentration pure formic acid solutions in an all-solid-state reactor. *Nat. Commun.* **11**, 3633 (2020).
49. L. Fan, F. Li, T. Liu, J. E. Huang, R. Miao, Y. Yan, S. Feng, C. Tai, S. Hung, H. Tsai, M. Chen, Y. Bai, D. Kim, S. Park, P. Papangelakis, C. Wu, A. S. Zeraati, R. Dorakhan, L. Sun, D. Sinton, E. Sargent, Atomic-level Cu active sites enable energy-efficient CO_2 electroreduction to multicarbon products in strong acid. *Nat. Synth.* **4**, 262–270 (2025).
50. D. Kim, S. Park, J. Lee, Y. Chen, F. Li, J. Kim, Y. Bai, J. E. Huang, S. Liu, E. D. Jung, B. Lee, P. Papangelakis, W. Ni, T. Alkayyali, R. Miao, P. Li, Y. Liang, A. S. Zeraati, R. Dorakhan, D. M. Meira, Y. Chen, D. Sinton, M. Zhong, E. H. Sargent, Acid-stable Cu cluster precatalysts enable high energy and carbon efficiency in CO_2 electroreduction. *J. Am. Chem. Soc.* **146**, 27701–27712 (2024).
51. H. Deng, T. Liu, W. Zhao, J. Wang, Y. Zhang, S. Zhang, Y. Yang, C. Yang, W. Teng, Z. Chen, G. Zheng, F. Li, Y. Su, J. Hui, Y. Wang, Substituent tuning of Cu coordination polymers enables carbon-efficient CO_2 electroreduction to multi-carbon products. *Nat. Commun.* **15**, 9706 (2024).
52. Y. Liang, F. Li, R. Miao, S. Hu, W. Ni, S. Zhang, Y. Liu, Y. Bai, H. Wan, P. Ou, X. Li, N. Wang, S. Park, F. Li, J. Zeng, D. Sinton, E. H. Sargent, Efficient ethylene electrosynthesis through C–O cleavage promoted by water dissociation. *Nat. Synth.* **3**, 1104–1112 (2024).
53. C. Zhao, G. Luo, X. Liu, W. Zhang, Z. Li, Q. Xu, Q. Zhang, H. Wang, D. Li, F. Zhou, Y. Qu, X. Han, Z. Zhu, G. Wu, J. Wang, J. Zhu, T. Yao, Y. Li, H. J. M. Bouwmeester, Y. Wu, In situ topotactic transformation of an interstitial alloy for CO electroreduction. *Adv. Mater.* **32**, e2002382 (2020).
54. G. Kresse, J. Hafner, Ab initio molecular dynamics for liquid metals. *Phys. Rev. B* **47**, 558–561 (1993).
55. J. P. Perdew, K. Burke, M. Ernzerhof, Generalized gradient approximation made simple. *Phys. Rev. Lett.* **77**, 3865–3868 (1996).
56. P. E. Blochl, Projector augmented-wave method. *Phys. Rev. B* **50**, 17953–17979 (1994).
57. K. Mathew, V. S. C. Kolluru, S. Mula, S. N. Steinmann, R. G. Hennig, Implicit self-consistent electrolyte model in plane-wave density-functional theory. *J. Chem. Phys.* **151**, 234101 (2019).
58. J. K. Nørskov, J. Rossmeisl, A. Logadottir, L. Lindqvist, J. R. Kitchin, T. Bligaard, H. Jónsson, Origin of the overpotential for oxygen reduction at a fuel-cell cathode. *J. Chem. Phys. B* **108**, 17886–17892 (2004).
59. S. Maintz, V. L. Deringer, A. L. Tchougréeff, R. Dronskowski, LOBSTER: A tool to extract chemical bonding from plane-wave based DFT. *J. Comput. Chem.* **37**, 1030–1035 (2016).
60. R. Nelson, C. Ertural, J. George, V. L. Deringer, G. Hautier, R. Dronskowski, LOBSTER: Local orbital projections, atomic charges, and chemical-bonding analysis from projector-augmented-wave-based density-functional theory. *J. Comput. Chem.* **41**, 1931–1940 (2020).
61. M. Lee, X. Li, A. Ozden, J. Wicks, P. Ou, Y. Li, R. Dorakhan, J. Lee, H. K. Park, J. W. Yang, B. Chen, J. Abed, R. dos Reis, G. Lee, J. E. Huang, T. Peng, Y. Chin, D. Sinton, E. H. Sargent, Selective synthesis of butane from carbon monoxide using cascade electrolysis and thermocatalysis at ambient conditions. *Nat. Catal.* **6**, 310–318 (2023).
62. K. Yue, Y. Qin, H. Huang, Z. Lv, M. Cai, Y. Su, F. Huang, Y. Yan, Stabilized Cu^0-Cu^{1+} dual sites in a cyanamide framework for selective CO_2 electroreduction to ethylene. *Nat. Commun.* **15**, 7820 (2024).
63. C. Dinh, T. Burdyny, M. G. Kibria, A. Seifitokaldani, C. M. Gabardo, F. P. G. de Arquer, A. Kiani, J. P. Edwards, P. D. Luna, O. S. Bushuyev, C. Zou, R. Q. Bermudez, Y. Pang, D. Sinton, E. H. Sargent, CO_2 electroreduction to ethylene via hydroxide-mediated copper catalysis at an abrupt interface. *Science* **360**, 783–787 (2018).
64. M. Sun, J. Cheng, M. Yamauchi, Gas diffusion enhanced electrode with ultrathin superhydrophobic macropore structure for acidic CO_2 electroreduction. *Nat. Commun.* **15**, 491 (2024).
65. J. Kang, Y. Wei, L. Liu, R. Han, B. Yu, J. Wang, Energy systems for climate change mitigation: A systematic review. *Appl. Energy* **263**, 114602 (2020).
66. C. Jin, Y. Lin, Y. Wang, J. Shi, R. Li, Y. Liu, Z. Yue, K. Leng, Y. Zhao, Y. Wang, X. Han, Y. Qu, J. Bai, Engineering atom-scale cascade catalysis via multi-active site collaboration for ampere-level CO_2 electroreduction to C_{2+} products. *Adv. Mater.* **37**, e2412658 (2025).
67. Y. Cao, Z. Chen, P. Li, A. Ozden, P. Ou, W. Ni, J. Abed, E. Shirzadi, J. Zhang, D. Sinton, J. Ge, E. H. Sargent, Surface hydroxide promotes CO_2 electrolysis to ethylene in acidic conditions. *Nat. Commun.* **14**, 2387 (2023).
68. W. Yang, Y. Zhao, Y. Chen, H. Ren, J. Sun, Z. Shi, X. Jin, Z. Zhang, X. Wang, Constraining CO_2 coverage on copper promotes CO_2 electroreduction to multi-carbon products in strong acid. *Angew. Chem. Int. Ed. Engl.* **64**, e202422082 (2025).
69. Y. Jiang, H. Li, C. Chen, Y. Zheng, S. Qiao, Dynamic Cu^0/Cu^+ interface promotes acidic CO_2 electroreduction. *ACS Catal.* **14**, 8310–8316 (2024).
70. S. Li, G. Wu, J. Mao, A. Chen, X. Liu, J. Zeng, Y. Wei, J. Wang, H. Zhu, J. Xia, X. Wang, G. Li, Y. Song, X. Dong, W. Wei, W. Chen, Tensile-strained Cu penetration electrode boosts asymmetric C–C coupling for ampere-level CO_2-to-C_{2+} reduction in acid. *Angew. Chem. Int. Ed. Engl.* **63**, e202407612 (2024).
71. J. Huang, X. Qiu, Z. Zhao, H. Zhu, Y. Liu, W. Shi, P. Liao, X. Chen, Single-product faradaic efficiency for electrocatalytic of CO_2 to CO at current density larger than 1.2 A cm^{-2} in neutral aqueous solution by a single-atom nanozyme. *Angew. Chem. Int. Ed. Engl.* **61**, e202210985 (2022).
72. J. Yi, X. Gao, H. Zhou, W. Chen, Y. Wu, Design of Co-Cu diatomic site catalysts for high-efficiency synergistic CO_2 electroreduction at industrial-level current density. *Angew. Chem. Int. Ed. Engl.* **61**, e202212329 (2022).
73. J. H. Lee, S. Kattel, Z. Jiang, Z. Xie, S. Yao, B. M. Tackett, X. We, N. S. Marinkovic, J. G. Chen, Tuning the activity and selectivity of electroreduction of CO_2 to synthesis gas using bimetallic catalysts. *Nat. Commun.* **10**, 3724 (2019).
74. Y. Chen, M. Xia, C. Zhou, Y. Zhang, C. Zhou, F. Xu, B. Feng, X. Wang, L. Yang, Z. Hu, Q. Wu, Hierarchical dual single-atom catalysts with coupled CoN_4 and NiN_4 moieties for industrial-level CO_2 electroreduction to syngas. *ACS Nano* **17**, 22095–22105 (2023).
75. H. Chen, K. Yang, T. Shao, D. Liu, H. Feng, S. Chen, C. A. Ortiz-Ledon, J. Duan, Q. Li, Augmented CO_2 utilization for acidic industrial-level CO_2 electroreduction to near-unity CO. *Electrochim. Acta* **469**, 143249 (2023).
76. X. Liu, M. T. M. Koper, Tuning the interfacial reaction environment for CO_2 electroreduction to CO in mildly acidic media. *J. Am. Chem. Soc.* **146**, 5242–5251 (2024).
77. B. Pan, J. Fan, J. Zhang, Y. Luo, C. Shen, C. Wang, Y. Wang, Y. Li, Close to 90% single-pass conversion efficiency for CO_2 electroreduction in an acid-fed membrane electrode assembly. *ACS Energy Lett.* **7**, 4224–4231 (2022).
78. J. Zhang, H. Jiang, X. Zhao, Z. Liu, L. Li, W. Ding, M. Zhong, Energy efficiency limit in CO-to-ethylene electroreduction and the method to advance towards. *Angew. Chem. Int. Ed. Engl.* **64**, e202502690 (2025).
79. R. Chen, H. Su, D. Liu, R. Huang, X. Meng, X. Cui, Z. Tian, D. Zhang, D. Deng, Highly selective production of ethylene by the electroreduction of carbon monoxide. *Angew. Chem. Int. Ed. Engl.* **59**, 154–160 (2020).
80. S. Wang, F. Li, J. Zhao, Y. Zeng, Y. Li, Z. Lin, T. Lee, S. Liu, X. Ren, W. Wang, Y. Chen, S. Hung, Y. Lu, Y. Cui, X. Yang, X. Li, Y. Huang, B. Liu, Manipulating C-C coupling pathway in electrochemical CO_2 reduction for selective ethylene and ethanol production over single-atom alloy catalyst. *Nat. Commun.* **15**, 10247 (2024).
81. Z. Jiang, Z. Zhang, H. Li, Y. Tang, Y. Yuan, J. Zao, H. Zheng, Y. Liang, Molecular catalyst with near 100% selectivity for CO_2 reduction in acidic electrolytes. *Adv. Energy Mater.* **13**, 2203603 (2023).
82. X. Sheng, W. Ge, H. Jiang, C. Li, Engineering the Ni-N-C catalyst microenvironment enabling CO_2 electroreduction with nearly 100% CO selectivity in acid. *Adv. Mater.* **34**, e2201295 (2022).
83. H. Li, L. Fang, T. Wang, R. Bai, J. Zhang, T. Li, Z. Duan, K. Chen, F. Pan, In situ modulated nickel single atoms on bicontinuous porous carbon fibers and sheets networks for acidic CO_2 reduction. *Adv. Mater.* **37**, 2416337 (2025).
84. T. Xu, H. Yang, T. Lu, R. Zhong, J. Lv, S. Zhu, M. Zhang, Z. Wang, Y. Yuan, J. Li, J. Wang, H. Jin, S. Pan, X. Wang, T. Cheng, S. Wang, Microenvironment engineering by targeted delivery of Ag nanoparticles for boosting electrocatalytic CO_2 reduction reaction. *Nat. Commun.* **16**, 977 (2025).

85. Z. Wang, W. Wang, Q. Yang, Y. Geng, Y. Du, K. Liu, Z. Wu, J. Lai, B. Li, H. Li, G. Zheng, L. Wang, Highly selective acidic CO_2 electroreduction with large current on polypyrrole-modified Ag catalyst by local microenvironment modulation. *Adv. Energy Mater.* **15**, 2405419 (2025).
86. J. Li, Y. Chen, B. Yao, W. Yang, X. Cui, H. Liu, S. Dai, S. Xi, Z. Sun, W. Chen, Y. Qin, J. Wang, Q. He, C. Ling, D. Wang, Z. Zhang, Cascade dual sites modulate local CO coverage and hydrogen-binding strength to boost CO_2 electroreduction to ethylene. *J. Am. Chem. Soc.* **146**, 5693–5701 (2024).
87. Y. Yao, T. Shi, W. Chen, J. Wu, Y. Fan, Y. Liu, L. Cao, Z. Chen, A surface strategy boosting the ethylene selectivity for CO_2 reduction and in situ mechanistic insights. *Nat. Commun.* **15**, 1257 (2024).
88. Z. Wei, W. Wang, T. Shao, S. Yang, C. Liu, D. Si, R. Cao, M. Cao, Constructing Ag/Cu_2O interface for efficient neutral CO_2 electroreduction to C_2H_4. *Angew. Chem. Int. Ed. Engl.* **64**, e202417066 (2025).
89. Z. Li, P. Wang, X. Lyu, V. K. R. Kondapalli, S. Xiang, J. D. Jimenez, L. Ma, T. Ito, T. Zhang, J. Raj, Y. Fang, Y. Bai, J. Li, A. Serov, V. Shanov, A. I. Frenkel, S. D. Senanayake, S. Yang, T. P. Senftle, J. Wu, Directing CO_2 electroreduction pathways for selective C_2 product formation using single-site doped copper catalysts. *Nat. Chem. Eng.* **1**, 159–169 (2024).
90. N. S. Romero Cuellar, C. Scherer, B. Kaçkar, W. Eisenreich, C. Huber, K. Wiesner-Fleischer, M. Fleischer, O. Hinrichsen, Two-step electrochemical reduction of CO_2 towards multi-carbon products at high current densities. *J. CO_2 Util.* **36**, 263–275 (2020).

Acknowledgments: We thank the Experimental Center of Engineering and Material Science in the University of Science and Technology of China. We thank the photoemission endstations BL1W1B in Beijing Synchrotron Radiation Facility (BSRF), BL14W1 in Shanghai Synchrotron Radiation Facility (SSRF), and BL10B and BL11U in National Synchrotron Radiation Laboratory (NSRL) for the help in characterizations. The artificial intelligence (AI)–driven experiments, simulations, and model training were performed on the robotic AI-Scientist platform of the Chinese Academy of Sciences. **Funding:** This work was supported by the China Ministry of Science and Technology (2021YFA1500404), the National Natural Science Foundation of China (224B2510, grant recipients: X.M.; 22422506, 22201271, 22221003, and 22425302, grant recipients: Y. Li), the Major Frontier Research Project of the University of Science and Technology of China (LS2060000002, grant recipients: Y.W. and H.Z.), the Joint Funds of the National Natural Science Foundation of China (U23A2081, grant recipients: Y.W.), the Anhui Provincial Key Research and Development Project (2023z04020010, grant recipients: Y.W.), the Anhui Provincial Natural Science Foundation (2108085UD06, grant recipients: Y.W.), the USTC Research Funds of the Double First-Class Initiative (YD2060006005, grant recipients: Y.W.), the Natural Science Foundation of Anhui Province (2208085UD04, grant recipients: H.Z.), and the China Ministry of Science and Technology (2021YFA1501003). **Author contributions:** Formal analysis: Y.S., W.J., J.Z., T.Y., Y.W., and Y.Li Validation: X.M., J.Z., W.J., Y.Lin, and Y.W. Software: W.J. and J.C. Resources: J.Z., H.Z., Y.Lin, and Y.W. Conceptualization: J.C., D.H., H.Z., Y.W., and X.M. Funding acquisition: J.C., H.Z., Y.W., and X.M. Methodology: J.Z., J.C., D.H., Y.W., Y.L., and X.M. Investigation: X.M., J.Z., and Y.Li Data curation: T.Y., Y.Lin, and X.M. Visualization: J.Z., C.C., and X.M. Supervision: Y.W. Writing—original draft: Y.W., H.Z., J.Z., and X.M. Writing—review and editing: Y.W., H.Z., X.M., W.J., and J.Z. Project administration: H.Z., Y.W., and X.M. **Competing interests:** The authors declare that they have no competing interests. **Data, code, and materials availability:** All data and code needed to evaluate and reproduce the results in the paper are present in the paper and/or the Supplementary Materials. This study did not generate new materials.

Submitted 1 July 2025
Accepted 10 April 2026
Published 13 May 2026
10.1126/sciadv.aea2538

ScienceAdvances

Acidic-alkaline tandem system for durable CO_2-CO-C_{2+}

Xianhui Ma, Juan Zhang, Dayin He, Wei Jiang, Yuanhua Sun, Jiayi Cui, Cai Chen, Yue Lin, Tao Yao, Huang Zhou, Yafei Li, and Yuen Wu

Sci. Adv. **12** (20), eaea2538. DOI: 10.1126/sciadv.aea2538